

Exploring muonphilic ALPs at muon colliders

Chih-Ting Lu¹, Xiaoyi Luo¹, Xinqi Wei¹

¹ *Department of Physics and Institute of Theoretical Physics,
Nanjing Normal University,
Nanjing, 210023, China*

(Dated: July 4, 2023)

Abstract

Axion-like particles (ALPs) are new particles that extend beyond the standard model (SM) and are highly motivated. When considering ALPs within an effective field theory framework, their couplings with SM particles can be studied independently. It is a daunting task to search for GeV-scale ALPs coupled to muons in collider experiments because their coupling is proportional to the muon mass. However, a recent study by Altmannshofer, Dror, and Gori (2022) highlighted the importance of a four-point interaction, $W\text{-}\mu\text{-}\nu\text{-}a$, as well as interactions from the chiral anomaly which couplings are not dependent on the muon mass. These interactions provide a new opportunity to explore muonphilic ALPs (μ ALPs) at the GeV scale. We have explored various μ ALPs production channels at muon colliders with μ ALPs decaying into a pair of muons. Especially, we found a pair of neutrinos accompanied by a μ ALP is a most effective channel to search for μ ALPs in the electroweak violating (EWW) scenario. In contrast, a photon plus a μ ALP becomes a better channel to search for μ ALPs in the electroweak preserving (EWP) scenario because there is no $W\text{-}\mu\text{-}\nu\text{-}a$ interaction in this situation. Most importantly, we found that the future bounds for μ ALPs in EWW scenario are much stronger than the ones in EWP scenario and the existing bounds for exploring μ ALPs with $1 \text{ GeV} \leq m_a \lesssim M_W$.

I. INTRODUCTION

Axion-like particles (ALPs) are predicted to exist in a wide range of models that extend beyond the standard model (SM). The QCD axion, introduced originally to solve the strong CP problem, is one such model [1–5]. ALPs can also be generated from different spontaneous symmetry breaking patterns of global symmetries [6–9] as well as in string theory [10–13] and models of extra dimensions [14, 15]. The broad spectrum of possible ALP masses makes them an attractive candidate for a variety of astrophysical and cosmological phenomena [16]. Sub-eV ALPs have been proposed as potential candidates for dark matter [17]. ALPs at different mass scales can also serve other purposes, such as acting as mediators to the dark sector [18, 19], influencing the structure of the electroweak phase transition [20, 21], and offering solutions to the hierarchy problem of the Higgs boson mass [22]. Understanding the characteristics and roles of ALPs is essential for unraveling the mysteries of the universe and advancing our knowledge of particle physics.

Various methods have been developed to search for ALPs, including laboratory-based experiments [23], astrophysical observations [24], and searches for ALPs in high-energy collisions [25]. The current constraints on ALPs rely on their coupling strength and mass. For example, astrophysical observations of the diffuse gamma-ray background provide tight constraints on the coupling strength of sub-eV ALPs to photons [26–29], while experiments based on the LEP and LHC can limit the coupling strength of high-mass ALPs to SM particles [30–35]. With the advancements of experimental techniques, these bounds are expected to become even more stringent in the future, offering exciting new prospects of investigating the properties of ALPs.

In this work, we focus on studying muonphilic ALPs (μ ALPs), a specific type of ALP that predominantly interacts with muons [36–43]. These ALPs can be considered in an effective field theory framework [25, 44–48], allowing us to study their couplings with SM particles independently. Bounds on μ ALPs for $m_a < 2m_\mu$ have already been obtained from searches in supernovae [36, 37, 40] and atmospheric air showers [41]. For $2m_\mu < m_a \lesssim \mathcal{O}(1)$ GeV, μ ALPs can be largely produced in fixed target experiments [18], low-energy e^+e^- colliders [49], and Tera Z factories [43]. However, searching for GeV-scale μ ALPs at high-energy colliders is challenging due to the small μ ALP production rate, as the coupling is proportional to the muon mass. Therefore, proposing new μ ALP production channels with

sufficiently large cross sections at high-energy colliders is crucial to search for GeV-scale μ ALPs.

Recently, a four-point interaction (W - ℓ - ν - a), which has a coupling that is independent of the charged lepton mass, has been proposed for the search of leptophilic ALPs [50]. This interaction is expected to arise from decays of π^\pm , K^\pm mesons, and the W boson, with the novel energy enhancement effect. Similarly, this kind of W - ℓ - ν - a interaction with energy enhancement effect has also been proposed as a promising approach for the search of leptophilic ALPs via t-channel processes ($\ell^+\ell^- \rightarrow \bar{\nu}_\ell a \nu_\ell$ and $\ell^- p \rightarrow \nu_\ell a j$) at high-energy colliders [51]. In this study, we investigated the production of GeV-scale μ ALPs from the above t-channel processes and their decay into a pair of muons at muon colliders [52–54]. Notably, when a light μ ALP is highly-boosted produced, the resulting pair of muons from the μ ALP decay is too collimated to pass the muon isolation criteria, and forms a novel object known as a muon-jet [58–69].

We investigate three major signal processes at muon colliders : $\mu^+\mu^- \rightarrow \nu_\mu a \bar{\nu}_\mu$, $\mu^+\mu^- \rightarrow \gamma a$ and $\mu^+\mu^- \rightarrow \mu^+\mu^- a$. These signal production modes mainly rely on a four-point interaction, W - μ - ν_μ - a , and/or interactions from the chiral anomaly which couplings are not dependent on the muon mass. Generally, $\mu^+\mu^- \rightarrow \nu_\mu a \bar{\nu}_\mu$ yields the largest cross section, followed by $\mu^+\mu^- \rightarrow \gamma a$ and $\mu^+\mu^- \rightarrow \mu^+\mu^- a$ in the electroweak violating (EWW) scenario. However, there is no W - μ - ν_μ - a interaction in the electroweak preserving (EWP) scenario, and therefore, $\mu^+\mu^- \rightarrow \gamma a$ yields the largest cross section. In the **EWW** scenario, we discovered that the channel $\mu^+\mu^- \rightarrow \nu_\mu a \bar{\nu}_\mu$ with the W - ℓ - ν - a interaction is the most important one among these channels because of its novel energy-enhancement behavior. Our findings suggest that searching for the signature of two isolated muons (or a muon-jet) plus missing energy in the **EWW** scenario at muon colliders can provide much stronger bounds than existing ones. On the other hand, searching for the signatures of two isolated muons (or a muon-jet) plus a photon and four isolated muons (or a muon-jet plus two isolated muons) in the **EWP** scenario at muon colliders may only slightly exceed existing bounds. Therefore, the muon collider is an ideal machine to search for μ ALPs and it can also explore a μ ALP belonging to the **EWW** or **EWP** scenario.

The plan of this paper is as follows. In Sec. II, we provide a brief review of ALP-muon interactions and μ ALP decay modes. The method to distinguish different ALP-muon interaction types using $\mu^+\mu^- \rightarrow \nu_\mu a \bar{\nu}_\mu$, $\mu^+\mu^- \rightarrow \gamma a$ and $\mu^+\mu^- \rightarrow \mu^+\mu^- a$ processes is discussed

in Sec. III. We present the results of a full signal-to-background analysis at muon colliders and compare them with existing bounds of the μ ALP in Sec. IV. Finally, we summarize our findings in Sec. V. Supplementary materials, including kinematic distributions for both signals and SM backgrounds and other tables are provided in Appendix A.

II. REVIEW ON ALP-MUON INTERACTIONS

We consider ALPs, generated from the global Peccei-Quinn (PQ) symmetry [1], $U(1)_{\text{PQ}}$, breaking. Based on the structure of the PQ symmetry, $a(x) \rightarrow a(x) + \text{const}$, the Lagrangian can be written in the form $\mathcal{L}_{\mu\text{ALP}} = \partial_\nu a J_{\text{PQ},\mu}^\nu$. The general muon current is in the form,

$$J_{\text{PQ},\mu}^\nu = \frac{c_\mu^V}{2\Lambda} \bar{\mu} \gamma^\nu \mu + \frac{c_\mu^A}{2\Lambda} \bar{\mu} \gamma^\nu \gamma_5 \mu + \frac{c_{\nu_\mu}}{2\Lambda} \bar{\nu}_\mu \gamma^\nu P_L \nu_\mu, \quad (1)$$

where Λ is the new physics scale, and c_μ^V , c_μ^A , c_{ν_μ} are dimensionless couplings. Without the assumption of electroweak invariance, the condition $c_{\nu_\mu} = c_\mu^V - c_\mu^A$ in Eq. (1) can be released¹. After integrating by parts of this Lagrangian, the $\mathcal{L}_{\mu\text{ALP}}$ can be written as [50]

$$\begin{aligned} a \partial_\nu J_{\text{PQ},\mu}^\nu = & i c_\mu^A \frac{m_\mu}{\Lambda} a \bar{\mu} \gamma_5 \mu + \frac{\alpha_{\text{em}}}{4\pi\Lambda} \left[\frac{c_\mu^V - c_\mu^A + c_{\nu_\mu}}{4s_W^2} a W_{\mu\nu}^+ \tilde{W}^{-,\mu\nu} \right. \\ & + \frac{c_\mu^V - c_\mu^A (1 - 4s_W^2)}{2s_W c_W} a F_{\mu\nu} \tilde{Z}^{\mu\nu} - c_\mu^A a F_{\mu\nu} \tilde{F}^{\mu\nu} + \\ & \left. \frac{c_\mu^V (1 - 4s_W^2) - c_\mu^A (1 - 4s_W^2 + 8s_W^4) + c_{\nu_\mu}}{8s_W^2 c_W^2} a Z_{\mu\nu} \tilde{Z}^{\mu\nu} \right] \\ & + \frac{ig_W}{2\sqrt{2}\Lambda} (c_\mu^A - c_\mu^V + c_{\nu_\mu}) a (\bar{\mu} \gamma^\nu P_L \nu_\mu) W_\nu^- + \text{h.c.}, \quad (2) \end{aligned}$$

the symbols $W_{\mu\nu}^\pm$, $Z_{\mu\nu}$, $F_{\mu\nu}$ represent the field strength tensors of massive gauge bosons W^\pm , Z and the massless photon, and the dual field strength tensor is defined as $\tilde{F}_{\mu\nu} = \frac{1}{2} \epsilon_{\mu\nu\rho\sigma} F^{\rho\sigma}$. On the other hand, α_{em} is the fine structure constant, g_W is the weak coupling constant and s_W and c_W are the sine and cosine of the weak mixing angle, respectively.

In Eq. (2), we label the first term as " **$a\mu\mu$** ", which can generate μ ALPs through the muon radiation. However, this term is suppressed by m_μ/Λ , necessitating high-intensity experiments to search for light μ ALPs. The second to the fourth terms, labeled as " **$a\mathbf{V}\mathbf{V}$** ", arise from the chiral anomaly and can produce light μ ALPs through flavor-changing processes in meson decays [48, 70, 71]. Heavier μ ALPs can also be produced from these terms

¹ Note the dimensional five operators with electroweak invariance to generate the first and the third terms in Eq. (1) are discussed in Ref. [50].

through gauge boson fusion and associated gauge boson production processes, despite not being proportional to m_μ , but having a $\alpha_{\text{em}}/4\pi$ suppression. The terms in the final line of Eq. (2), labeled as " $\mathbf{aW}\mu\nu$ ", are often overlooked in the literature [72]. However, they are critical to our work, particularly for searching for μ ALPs in the GeV scale. This four-point interaction, W - μ - ν_μ - a , vanishes when the general muon current in Eq. (1) respects the electroweak symmetry. Moreover, this interaction is not related to m_μ and has an obvious (energy/ Λ) enhancement in specific processes. This enhancement behavior is crucial in constraining light μ ALPs through decays of the W boson and charged mesons [50], as well as in searching for heavier μ ALPs in t -channel processes such as $\mu^+\mu^- \rightarrow \nu_\mu a \bar{\nu}_\mu$ at muon colliders under the EWV scenario which will be defined in the next section.

On the other hand, searching for μ ALPs in collider experiments will depend on their decay modes. For μ ALP masses below the electroweak scale ($m_a \lesssim M_W$), their dominant decay modes are to $\mu^+\mu^-$ and $\gamma\gamma$ [25, 45, 73]. The decay widths are given by

$$\Gamma_{a \rightarrow \mu^+\mu^-} = \frac{(c_\mu^A)^2 m_\mu^2 m_a}{8\pi\Lambda^2} \sqrt{1 - \frac{4m_\mu^2}{m_a^2}}, \quad \Gamma_{a \rightarrow \gamma\gamma} = \frac{g_{a\gamma\gamma}^2 m_a^3}{64\pi}, \quad (3)$$

where the coupling constant $g_{a\gamma\gamma}$ is determined by the chiral anomaly and one-loop triangle Feynman diagrams, and can be expressed as

$$g_{a\gamma\gamma} = \frac{\alpha_{\text{em}} c_\mu^A}{\pi \Lambda} \left| 1 - \mathcal{F}\left(\frac{m_a^2}{4m_\mu^2}\right) \right| \quad (4)$$

and the loop function $\mathcal{F}(z > 1) = \frac{1}{z} \arctan^2\left(\frac{1}{\sqrt{1/z-1}}\right)$. Here, we only consider the contribution from the muon loop, as the contribution from the W boson is strongly suppressed and can be safely neglected.

The Fig. 1 shows the branching ratios for $a \rightarrow \mu^+\mu^-$ and $a \rightarrow \gamma\gamma$. When $m_a \lesssim M_W$, the dominant decay mode of μ ALP is $a \rightarrow \mu^+\mu^-$. Since the partial decay width of $a \rightarrow \gamma\gamma$ depends slightly on the muon mass and scales with m_a^3 , we can expect the branching ratio of $a \rightarrow \gamma\gamma$ to increase with the μ ALP mass. It is important to note that this result is opposite to that of the electrophilic ALP in Ref. [51] because the muon mass is much larger than the electron mass.

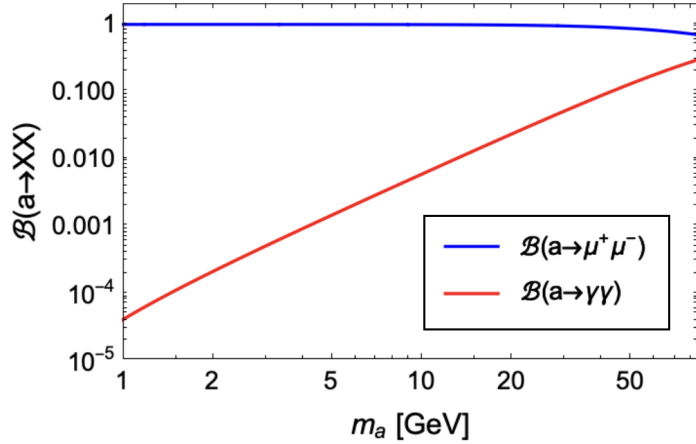


FIG. 1: The decay branching ratios of μ ALP below the electroweak scale ($m_a \lesssim M_W$).

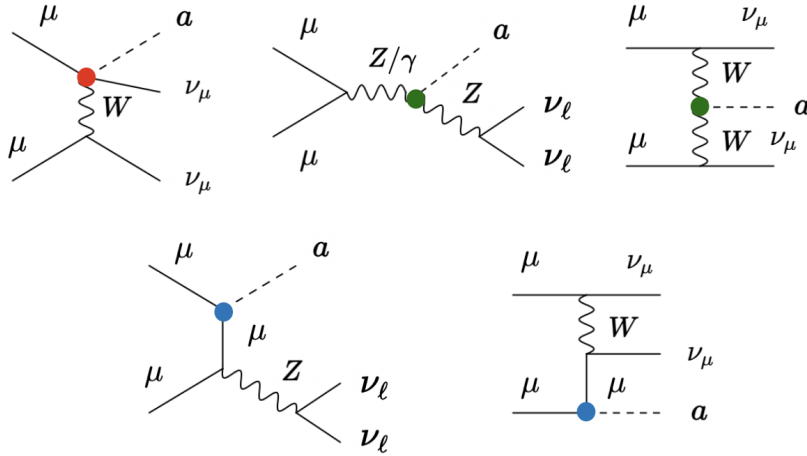


FIG. 2: Feynman diagrams for $\mu^+\mu^- \rightarrow \nu_\mu a \bar{\nu}_\mu$. Here the color markers indicate red for $aW\mu\nu$ interaction, green for aVV' interaction and blue for $a\mu\mu$ interaction.

III. DISTINGUISH DIFFERENT ALP-MUON INTERACTION TYPES AT MUON COLLIDERS

In this section, we focus on distinguishing between different types of ALP-muon interactions at muon colliders. First, we consider the signal process $\mu^+\mu^- \rightarrow \nu_\mu a \bar{\nu}_\mu$ with the relevant Feynman diagrams showing in Fig. 2 and numerically investigate the energy enhancement behavior of this process at muon colliders. To implement $\mathcal{L}_{\mu\text{ALP}}$ from Eq. (2), we use FeynRules [74] and calculate cross sections for this process using Madgraph5_aMC@NLO [75],

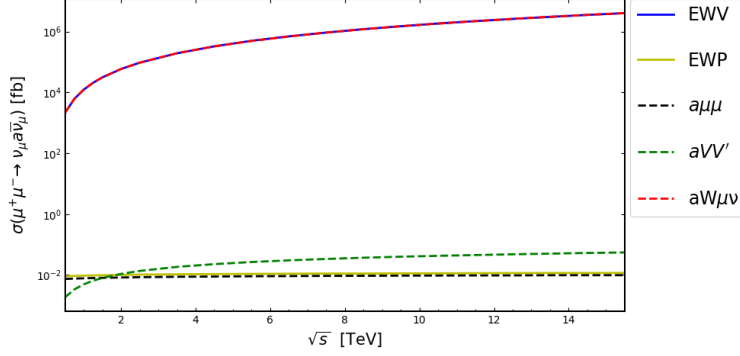


FIG. 3: The energy enhancement behavior of cross sections in $\mu^+\mu^- \rightarrow \nu_\mu a \bar{\nu}_\mu$ with $m_a = 10$ GeV, $c_\mu^A/\Lambda = 10$ TeV $^{-1}$, $c_\mu^V = c_{\nu_\mu} = 0$ (**EWV**: solid-blue line) and $c_\mu^A/\Lambda = c_\mu^V/\Lambda = 10$ TeV $^{-1}$, $c_{\nu_\mu} = 0$ (**EWP**: solid-olive line). In the **EWV** scenario, the dashed-red, dashed-green, and dashed-black lines are labeled as contributions from $\mathbf{aW}\mu\nu$, \mathbf{aVV}' and $\mathbf{a}\mu\mu$ interactions, respectively.

while varying the center-of-mass energy. As we know, the condition $c_{\nu_\mu} = c_\mu^V - c_\mu^A$ is a criterion to determine whether the ALP effective field theory is electroweak invariant or not. Therefore, we set $c_\mu^A/\Lambda = 10$ TeV $^{-1}$ and $c_\mu^V = c_{\nu_\mu} = 0$ as a benchmark point for the electroweak violating (**EWV**) scenario. Similarly, we set $c_\mu^A/\Lambda = c_\mu^V/\Lambda = 10$ TeV $^{-1}$ and $c_{\nu_\mu} = 0$ as a benchmark point for the electroweak preserving (**EWP**) scenario. We vary the center-of-mass energy \sqrt{s} between 1 – 15 TeV with $m_a = 10$ GeV at muon colliders. Fig. 3 shows the energy enhancement behavior of cross section in $\mu^+\mu^- \rightarrow \nu_\mu a \bar{\nu}_\mu$, where the full contributions from the **EWV** and **EWP** scenarios are depicted in solid lines, and the contributions from $\mathbf{aW}\mu\nu$, \mathbf{aVV}' , and $\mathbf{a}\mu\mu$ in the **EWV** scenario are depicted in dashed lines.

As shown in Fig. 3, the leading contribution in the **EWV** scenario comes from the $\mathbf{aW}\mu\nu$ interaction, with the subleading contribution from \mathbf{aVV}' interaction. The contribution from \mathbf{aVV}' interaction is about seven orders of magnitude smaller than that from $\mathbf{aW}\mu\nu$, as depicted in dashed lines in Fig. 3. For $\sqrt{s} = 1 - 2$ TeV, the energy enhancement behaviors from these two interactions are evident because the momentum transfer size becomes large enough, making $\mathbf{aW}\mu\nu$ and \mathbf{aVV}' interactions important. However, as energy continues to increase, the growth rate becomes gentler because these two leading contributions steadily increase with the center-of-mass energy as (energy/ Λ).

Our numerical analysis reveals that the contribution from the $\mathbf{aW}\mu\nu$ interaction is much

greater than those from the \mathbf{aVV}' and $\mathbf{a}\mu\mu$ interactions because of the novel energy enhancement behavior. Therefore, we show the analytical form for the amplitude square with the average (sum) over initial (final) polarization for the $\mathbf{aW}\mu\nu$ interaction in the process $\mu^+(p_1)\mu^-(p_2) \rightarrow \nu_\mu(q_1)a(q_2)\bar{\nu}_\mu(q_3)$,

$$\begin{aligned} |\overline{\mathcal{M}}|^2 &= \frac{g_W^4 (c_\mu^A - c_\mu^V + c_{\nu_\mu})^2}{32\Lambda^2} \left(\frac{1}{k^2 - M_W^2} + \frac{1}{k'^2 - M_W^2} \right)^2 \\ &\quad \times (s - 2m_\mu^2) [s - m_a^2 - 2q_2 \cdot (q_1 + q_3)] , \end{aligned}$$

where $s = (p_1 + p_2)^2 = (q_1 + q_2 + q_3)^2$, $k = p_2 - q_3$ and $k' = p_1 - q_1$. It shows that the amplitude square can be enhanced when the momentum transfer in the t -channel process is large enough.

In the **EWV** scenario, the contribution from $\mathbf{a}\mu\mu$ interaction is negligible, while in the **EWP** scenario, there are both \mathbf{aVV}' and $\mathbf{a}\mu\mu$ interactions in $\mu^+\mu^- \rightarrow \nu_\mu a \bar{\nu}_\mu$. The cross sections have no obvious change with the center-of-mass energy increase in the **EWP** scenario due to the lack of energy enhancement effect. Lastly, the cross sections in the **EWV** scenario are more than six orders of magnitude larger than those in the **EWP** scenario for $\mu^+\mu^- \rightarrow \nu_\mu a \bar{\nu}_\mu$ process in Fig. 3. This is because there is $\mathbf{aW}\mu\nu$ interaction in the **EWV** scenario, but not in the **EWP** scenario, and this interaction contributes to almost the entire cross-section amount in the **EWV** scenario. Therefore, this process is powerful to distinguish μ ALPs in the **EWV** scenario from the **EWP** scenario.

production channel	cross section [fb]	
	EWV	EWP
$\mu^+\mu^- \rightarrow \nu_\mu a \bar{\nu}_\mu$	3.13×10^4	9.69×10^{-3}
$\mu^+\mu^- \rightarrow \mu^+\mu^- a$	1.45×10^{-2}	1.69×10^{-2}
$\mu^+\mu^- \rightarrow a\gamma$	7.72×10^{-2}	8.18×10^{-2}
$\mu^+\mu^- \rightarrow Za$	3.58×10^{-3}	2.54×10^{-2}

TABLE I: The cross sections of different μ ALP production channels at a muon collider with $\sqrt{s} = 3$ TeV has been shown in this table with the benchmark point $m_a = 10$ GeV and $c_\mu^A/\Lambda = 10$ TeV $^{-1}$.

Next, we discuss four optimal channels for searching for μ ALPs at a muon collider.

Among these channels, we specifically consider those μ ALP couplings which are independent of the muon mass. These μ ALP production channels are $\mu^+\mu^- \rightarrow \nu_\mu a \bar{\nu}_\mu$, $\mu^+\mu^- \rightarrow \gamma a$, $\mu^+\mu^- \rightarrow \mu^+\mu^- a$ and $\mu^+\mu^- \rightarrow Z a$. To compare these μ ALP production channels at a muon collider with $\sqrt{s} = 3$ TeV, we calculated their cross sections in both **EWV** and **EWP** scenarios with the benchmark point $m_a = 10$ GeV and $c_\mu^A/\Lambda = 10$ TeV⁻¹, as shown in Table I. In the **EWV** scenario, we found that the $\mu^+\mu^- \rightarrow \nu_\mu a \bar{\nu}_\mu$ channel has the largest cross section, due to its energy-enhancing behavior caused by the W - μ - ν_μ - a interaction. The cross section of this channel is about six to seven orders of magnitude higher than that of other channels. However, in the **EWP** scenario, there is no energy-enhancing behavior in the $\mu^+\mu^- \rightarrow \nu_\mu a \bar{\nu}_\mu$ channel such that the cross section of this channel becomes smaller than that of other channels. At this point, the cross section of the $\mu^+\mu^- \rightarrow \gamma a$ channel is the largest, making it the most prospective search channel in the **EWP** scenario.

IV. SIGNAL-TO-BACKGROUND ANALYSIS AT A MUON COLLIDER

In this section, we investigate signal and background analysis on three specific search channels: $\mu^+\mu^- \rightarrow \nu_\mu a \bar{\nu}_\mu$, $\mu^+\mu^- \rightarrow \gamma a$ and $\mu^+\mu^- \rightarrow \mu^+\mu^- a$ processes. Our goal is to predict the future bounds for GeV-scale μ ALPs at a muon collider and compare them with existing bounds.

A. Exploring $\mu^+\mu^- \rightarrow \nu_\mu a \bar{\nu}_\mu$ in the EWV scenario

As an illustration, we analyze the process $\mu^+\mu^- \rightarrow \nu_\mu a \bar{\nu}_\mu$ in the **EWV** scenario and its relevant SM backgrounds in the context of the popular muon collider proposal with $\sqrt{s} = 3$ TeV [53, 54]. According to Fig. 1, the μ ALP mainly decays to $\mu^+\mu^-$ when $m_a \lesssim M_W$. Hence, we focus on the $a \rightarrow \mu^+\mu^-$ decay mode in our analysis. The μ ALP becomes highly boosted at the muon collider when it is light enough, so $\mu^+\mu^-$ in the final state may be too collimated to pass the muon isolation criterion at detectors. Taking a cone size $R = 0.1$ as the muon isolation criterion at the muon collider, we find a pair of muons cannot be isolated to each other at detectors when $m_a \lesssim 15$ GeV (parton-level) in the left panel of Fig. 4. We can group this kind of collimated, non-isolated muons as a special signature "muon-jet" (J_μ) which is a non-QCD jet-like structure and deposits most of its energy in the the muon

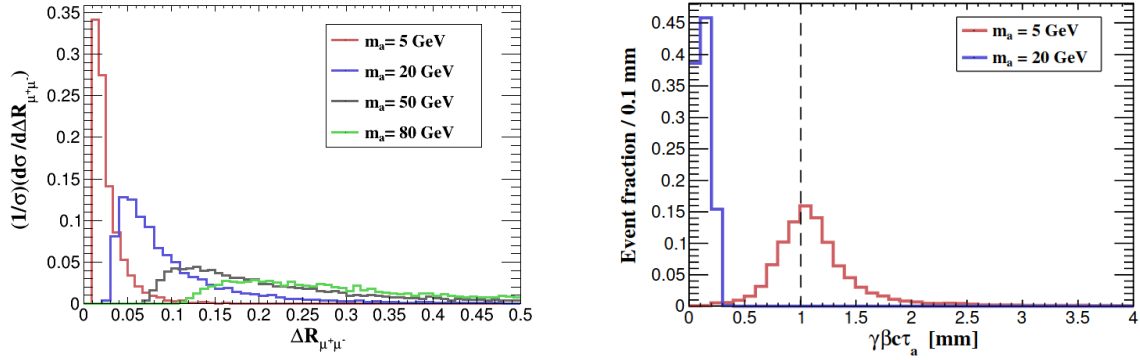


FIG. 4: Left panel : Distribution of the opening angle between two muons, $\Delta R_{\mu^+\mu^-}$, from $\mu^+\mu^- \rightarrow \nu_\mu a \bar{\nu}_\mu$ at the muon collider with $\sqrt{s} = 3$ TeV. Four benchmark mass values of μ ALP, $m_a = 5, 20, 50, 80$ GeV are displayed. Right panel : Distribution of the μ ALP lab frame decay length from $\mu^+\mu^- \rightarrow \nu_\mu a \bar{\nu}_\mu$ at the muon collider with $\sqrt{s} = 3$ TeV. The benchmark points $m_a = 5, 20$ GeV with $c_\mu^A/\Lambda = 0.1 \text{ TeV}^{-1}$ are considered.

spectrometer and has distinct signature from QCD jets. Therefore, we classify the signal signatures into two categories: (1) two isolated muons plus missing energy (\cancel{E}) for $m_a \gtrsim 15$ GeV, and (2) a J_μ plus \cancel{E} for $m_a \lesssim 15$ GeV.

cut flow in σ [fb]	signal	$\nu_\ell \bar{\nu}_\ell \mu^+ \mu^-$	$t\bar{t}$
Generator	2.54	162.70	4.15×10^{-2}
cut-(1)	1.78	18.60	7.94×10^{-3}
cut-(2)	1.78	11.28	7.21×10^{-3}
cut-(3)	1.78	11.27	3.54×10^{-4}
cut-(4)	1.74	0.15	2.12×10^{-5}
cut-(5)	1.47	1.23×10^{-2}	8.30×10^{-7}
cut-(6)	1.35	6.17×10^{-3}	0

TABLE II: The cut-flow table for $\mu^+\mu^- \rightarrow \nu_\ell(a \rightarrow \mu^+\mu^-)\bar{\nu}_\ell$ and relevant SM backgrounds with signature of two isolated muons plus \cancel{E} . The benchmark point $m_a = 50$ GeV with $c_\mu^A/\Lambda = 0.1 \text{ TeV}^{-1}$ for signal is chosen. Each event selection has been mentioned in the

main text. The "Generator" means the cross sections in parton-level calculated by

Madgraph5_aMC@NLO.

For the first signal signature, two relevant SM backgrounds : $\mu^+\mu^- \rightarrow \nu_\ell\bar{\nu}_\ell\mu^+\mu^-$ and $\mu^+\mu^- \rightarrow t\bar{t} \rightarrow (b\mu^+\nu_\mu)(\bar{b}\mu^-\bar{\nu}_\mu)$ are considered. We choose the benchmark point $m_a = 50$ GeV with $c_\mu^A/\Lambda = 0.1 \text{ TeV}^{-1}$ to display the signal features. To generate Monte Carlo samples for both signal and background processes, we use Madgraph5_aMC@NLO [75] and pass them to Pythia8 [76] for QED and QCD showering and hadronization effects. We impose pre-selection cuts ($P_T^\mu > 5$ GeV and $|\eta_\mu| < 2.5$) at the parton-level for both the signal and backgrounds. To simulate the detector effects, we use the muon collider template in Delphes3 [77] which the muon isolation criterion is consistent with Ref. [78, 79]. We use the Cambridge/Aachen (C/A) jet clustering algorithm [80, 81] and consider a b-jet tagging efficiency of $\epsilon_b = 0.8$ with charm-jet and light-jet fake rates of $P_{c \rightarrow b} = 0.1$ and $P_{j \rightarrow b} = 10^{-3}$, respectively. The following event selections to identify the signal signature and suppress background events are required :

- (1) $N(\mu) \geq 2$ with $P_T^{\mu_1} > 200$ GeV, $P_T^{\mu_2} > 10$ GeV, $|\eta_{\mu_{1,2}}| < 1.5$,
- (2) $1500 < \cancel{E} < 2800$ GeV and $|\eta_{\cancel{E}}| < 1.8$,
- (3) Veto $N(b) \geq 1$ GeV with $P_T^b > 25$ GeV,
- (4) $\cancel{E}/M_{\mu_1\mu_2} > 32$,
- (5) $|M_{\mu_1\mu_2} - m_a| < 2$ GeV,
- (6) $3.0 < \Delta\phi_{\mu_1, \cancel{E}} < 3.3$ and $2.9 < \Delta\phi_{\mu_2, \cancel{E}} < 3.5$,

where $P_T^{\mu_1}$, $P_T^{\mu_2}$ (η_{μ_1} , η_{μ_2}) are the transverse momentum (pseudorapidity) of leading and subleading energetic muons, \cancel{E} is the missing energy, $M_{\mu_1\mu_2}$ is the invariant mass of a muon pair, $\Delta\phi_{\mu_i, \cancel{E}}$ is the azimuthal angle between the i-th muon and \cancel{E} . The cut-flow table including signal and backgrounds for each event selection is listed in Table. II and some kinematic distributions are shown in Fig. 7 of Appendix A.

First, we found two isolated muons and \cancel{E} in the central region of signal events. To select candidate events, we applied the following trigger criteria : $P_T^{\mu_1} > 200$ GeV, $P_T^{\mu_2} > 10$ GeV, and $\cancel{E} > 1500$ GeV. In Fig. 7, the distributions of $P_T^{\mu_1}$ and \cancel{E} show two peaks that correspond to the $\mu^+\mu^- \rightarrow \nu_\ell\bar{\nu}_\ell\mu^+\mu^-$ process. The right peak of \cancel{E} distribution indicates that most of the energy is carried away by the neutrino pair, leaving minimal energy for the two muons, while the left peak indicates that each of the two muons and two neutrinos

carries almost an equal share of the energy. For the $\mu^+\mu^- \rightarrow t\bar{t} \rightarrow (b\mu^+\nu_\mu)(\bar{b}\mu^-\bar{\nu}_\mu)$ process, the \cancel{E} distribution peak is around 2600 GeV, indicating that the two neutrinos take away more energy. As the signal \cancel{E} distribution peak is around 2000 GeV, we applied $\cancel{E} < 2800$ GeV to reduce these two background events. Moreover, to suppress the b jet background from the $\mu^+\mu^- \rightarrow t\bar{t} \rightarrow (b\mu^+\nu_\mu)(\bar{b}\mu^-\bar{\nu}_\mu)$ process, we vetoed events with $N(b) \geq 1$ GeV and $P_T^b > 25$ GeV. We also applied the ratio $\cancel{E}/M_{\mu_1\mu_2}$ as a complementary selection for the μ ALP mass window, setting $\cancel{E}/M_{\mu_1\mu_2} > 32$. This selection was based on the observation that the position of the average $M_{\mu_1\mu_2}$ distribution of the $\mu^+\mu^- \rightarrow \nu_\ell\bar{\nu}_\ell\mu^+\mu^-$ process is larger than that of the signal, and the \cancel{E} distribution from this background is relatively small in the range $1500 < \cancel{E} < 2800$ GeV. The μ ALP mass window selection effectively reduced these two backgrounds while keeping most of the signal events. By applying the cuts of $\Delta\phi_{\mu_1,2,\cancel{E}}$ to reduce some events from $\mu^+\mu^- \rightarrow \nu_\ell\bar{\nu}_\ell\mu^+\mu^-$, we observed that two isolated muons were well-separated from \cancel{E} . Especially, the distribution of $\Delta\phi_{\mu_2,\cancel{E}}$ is not so large in both $\mu^+\mu^- \rightarrow \nu_\ell\bar{\nu}_\ell\mu^+\mu^-$ and $\mu^+\mu^- \rightarrow t\bar{t} \rightarrow (b\mu^+\nu_\mu)(\bar{b}\mu^-\bar{\nu}_\mu)$ compared to the signal. Finally, using a benchmark integrated luminosity $\mathcal{L} = 120 \text{ fb}^{-1}$ of a muon collider, we defined the signal significance Z [82] as

$$Z = \sqrt{2 \cdot ((N_s + N_b) \cdot \ln(1 + N_s/N_b) - N_s)}, \quad (5)$$

where N_s and N_b are the relevant signal and background event numbers. Here the systematic uncertainties are not taken into account in our simple analysis since the muon collider is still a future collider. After all of these event selections in Table. II, we find the signal significance can reach $Z = 38$ for our benchmark point of $\mathcal{L} = 120 \text{ fb}^{-1}$ which means $c_\mu^A/\Lambda < 0.1 \text{ TeV}^{-1}$ is still detectable in the future.

In the above analysis, we consider the prompt μ ALP decay with the lab frame decay length, $\gamma\beta c\tau_a < 1 \text{ mm}$ as a criterion at a muon collider. Here, γ is the Lorentz factor, β is the μ ALP velocity, and τ_a is the proper decay time of μ ALP. However, as we can expect, the μ ALP lab frame decay length becomes longer when m_a , c_μ^A/Λ are small, and β is large. In this situation, μ ALPs become long-lived particles (LLPs). We take two benchmark points, $m_a = 5, 20 \text{ GeV}$ with $c_\mu^A/\Lambda = 0.1 \text{ TeV}^{-1}$, to display the $\gamma\beta c\tau_a$ distribution from $\mu^+\mu^- \rightarrow \nu_\mu a \bar{\nu}_\mu$ at the muon collider in the right panel of Fig. 4. We will discuss the situation of μ ALPs as the LLPs later in Sec. IV C.

For the second signal signature, possible SM backgrounds come from $\nu_\ell\bar{\nu}_\ell b\bar{b}$ and $\nu_\ell\bar{\nu}_\ell c\bar{c}$

cut flow in σ [fb]	signal	$\nu_\ell \bar{\nu}_\ell c \bar{c}$	$\nu_\ell \bar{\nu}_\ell b \bar{b}$
Generator	2.73	208.20	633.60
$\gamma\beta c\tau_a < 1$ mm	0.52	—	—
cut-(1)	0.50	4.86×10^{-3}	0.17
cut-(2)	0.50	1.39×10^{-3}	2.41×10^{-2}
cut-(3)	0.47	0	6.31×10^{-3}
cut-(4)	0.47	0	1.27×10^{-3}
cut-(5)	0.42	0	0

TABLE III: Similar to Table. II, but for the signal benchmark point $m_a = 5$ GeV and $c_\mu^A/\Lambda = 0.1$ TeV $^{-1}$ as well as the signature of a J_μ candidate plus \cancel{E} .

where the heavy flavor mesons produced from c , b jets can decay to a collimated muon pair and mimic the J_μ from the signal. The pre-selection cuts ($P_T^\mu > 5$ GeV, $|\eta_\mu| < 2.5$) at parton-level have been used for signal and background processes. We take the signal benchmark point as $m_a = 5$ GeV and $c_\mu^A/\Lambda = 0.1$ TeV $^{-1}$. The C/A jet clustering algorithm for J_μ with a cone size $R = 0.1$ which corresponds to the muon isolation criterion at the muon collider is applied. We set up event selections to identify the signal signature and suppress the background events below :

- (1) $N(\mu) \geq 2$ with $P_T^{\mu_{1,2}} > 5$ GeV, $|\eta_{\mu_{1,2}}| < 2.5$,
- (2) $N(J_\mu) = 1$ and $P_T^{J_\mu} > 20$ GeV, $|\eta_{J_\mu}| < 2$,
- (3) $1500 < \cancel{E} < 2800$ GeV and $|\eta_{\cancel{E}}| < 1.4$,
- (4) Veto $N(b) \geq 1$ GeV with $P_T^b > 25$ GeV,
- (5) $|M_{J_\mu} - m_a| < 2$ GeV.

The cut-flow table including signal and backgrounds for each event selection is listed in Table. III and some kinematic distributions are shown in Fig. 8 of Appendix A.

For the μ ALP prompt decay, we first set $\gamma\beta c\tau_a < 1$ mm as a criterion. Then, two muons with $P_T^\mu > 5$ GeV and $|\eta_\mu| < 2.5$ are required to be detectable in the muon spectrometer. We consider a J_μ candidate with $P_T^{J_\mu} > 20$ GeV and $\cancel{E} > 1500$ GeV as the trigger, which

are mainly distributed in the central region. The J_μ in signal events comes from energetic μ ALPs, whereas in background events, it comes from the decay of heavy flavor mesons. As shown in Fig. 8, the $P_T^{J_\mu}$ of the signal is much larger than that of those backgrounds, and most of the background events have been largely reduced after the cut-(2). We further require the selection $\cancel{E} < 2800$ GeV, which retains most signal events while removing significant parts of background events, particularly the events from $\mu^+\mu^- \rightarrow \nu_\ell \bar{\nu}_\ell c\bar{c}$ have been entirely removed. To suppress $\mu^+\mu^- \rightarrow \nu_\ell \bar{\nu}_\ell b\bar{b}$, we veto $N(b) \geq 1$ GeV with $P_T^b > 25$ GeV. We also require the jet mass of J_μ to satisfy the μ ALP mass window selection, which can entirely remove events from $\mu^+\mu^- \rightarrow \nu_\ell \bar{\nu}_\ell b\bar{b}$. After all event selections in Table. III, we can take this signal benchmark point as background-free. The distribution of the peak of M_{J_μ} is broader than that of $M_{\mu_1\mu_2}$ because two muons within a J_μ cannot pass the muon isolation criteria. The selection of the jet clustering method, in conjunction with the choice of cone size $R = 0.1$, can affect the four-momentum reconstruction of the J_μ . In some cases, one of the muons is outside the jet cone and cannot be reconstructed, leading to distortions in M_{J_μ} compared to $M_{\mu_1\mu_2}$. With $\mathcal{L} = 120 \text{ fb}^{-1}$, there are 50 signal events left for this benchmark point after all event selections.

B. Exploring $\mu^+\mu^- \rightarrow \gamma a$ and $\mu^+\mu^- \rightarrow \mu^+\mu^- a$ in the EWP scenario

In the **EWP** scenario, we employ a different approach to search for μ ALPs compared to the **EWV** scenario. As explained towards the end of Sec. III, $\mu^+\mu^- \rightarrow \nu_\mu a \bar{\nu}_\mu$ process in the **EWP** scenario lacks energy-enhancement behavior, leading to a smaller production cross section. For this reason, we have opted to focus on the following two μ ALP production channels, $\mu^+\mu^- \rightarrow \gamma a$ and $\mu^+\mu^- \rightarrow \mu^+\mu^- a$, which have larger production cross sections, for the signal-to-background analyses in order to obtain stronger future bounds. We analyzed the process $\mu^+\mu^- \rightarrow \gamma a$ ($a \rightarrow \mu^+\mu^-$) using the same method as Sec. IV A. The details and results are presented below. The signal signatures are first classified into two categories : (1) two isolated muons plus a photon (γ) for $m_a \gtrsim 15$ GeV, and (2) a J_μ plus a γ for $m_a \lesssim 15$ GeV. To investigate the first signal signature, we consider the relevant SM background : $\mu^+\mu^- \rightarrow \gamma \mu^+\mu^-$ and choose the benchmark point $m_a = 50$ GeV with $c_\mu^A/\Lambda = 10 \text{ TeV}^{-1}$ to display the signal features. The following event selections to identify the signal signature and suppress background events are required :

cut flow in σ [fb]	signal	$\mu^+\mu^- \rightarrow \gamma\mu^+\mu^-$
Generator	6.84×10^{-2}	179.80
cut-(1)	2.70×10^{-2}	4.72
cut-(2)	2.69×10^{-2}	0.98
cut-(3)	2.48×10^{-2}	0.56
cut-(4)	2.03×10^{-2}	2.70×10^{-2}
cut-(5)	1.68×10^{-2}	3.06×10^{-3}

TABLE IV: The cut-flow table for $\mu^+\mu^- \rightarrow \gamma a$ and the relevant SM background with the signature of two isolated muons plus a photon. The benchmark point $m_a = 50$ GeV with $c_\mu^A/\Lambda = 10 \text{ TeV}^{-1}$ for the signal is chosen.

- (1) $N(\mu) \geq 2$ with $P_T^{\mu_1} > 100$ GeV, $10 < P_T^{\mu_2} < 500$ GeV, $|\eta_{\mu_{1,2}}| < 1.5$,
- (2) $E_\gamma > 1450$ GeV and $|\eta_\gamma| < 1.6$,
- (3) $2.9 < \Delta\phi_{\mu_1,\gamma} < 3.4$ and $2.9 < \Delta\phi_{\mu_2,\gamma} < 3.3$,
- (4) $E_\gamma/M_{\mu_1\mu_2} > 29$,
- (5) $|M_{\mu_1\mu_2} - m_a| < 2.0$ GeV.

where E_γ is the energy of photon, $\Delta\phi_{\mu_i,\gamma}$ is the azimuthal angle between the i -th muon and the photon. The cut-flow table detailing the signal and background for each event selection is presented in Table IV, with some relevant kinematic distributions shown in Fig. 9 of Appendix A. First, we found that two isolated muons in the signal is predominantly located in the relatively low transverse momentum regions (as shown in Fig. 9), whereas the number of signal events for E_γ is mainly located in the relatively higher energy regions. This is because two muons in the signal are produced from the decay of the μ ALP, which are secondary particles. By contrast, two muons from the background events mainly come from the initial particles. Similarly, the photon in the signal is produced from the initial muons and therefore becomes more energetic. On the other hand, for the background process, the energy of photons is more divided by the P_z of muons, so the leading photon energy is smaller than that of the signal process as shown in Fig. 9. To select candidate

cut flow in σ [fb]	signal	$\gamma c\bar{c}$	$\gamma b\bar{b}$
Generator	8.03×10^{-2}	5.96	8.48
cut-(1)	7.78×10^{-2}	4.70×10^{-3}	1.78×10^{-2}
cut-(2)	6.36×10^{-2}	7.63×10^{-4}	5.49×10^{-4}
cut-(3)	5.29×10^{-2}	1.19×10^{-5}	1.50×10^{-4}
cut-(4)	4.43×10^{-2}	0	1.33×10^{-4}
cut-(5)	3.61×10^{-2}	0	4.99×10^{-5}

TABLE V: Similar to Table. IV, but for the signal benchmark point $m_a = 5$ GeV and $c_\mu^A/\Lambda = 10$ TeV $^{-1}$ as well as the signature of a J_μ candidate plus a photon.

events, we applied the following trigger criteria: $P_T^{\mu_1} > 100$ GeV, $P_T^{\mu_2} > 10$ GeV, and $E_\gamma > 1450$ GeV. To reduce background events, we apply the cut of $\Delta\phi_{\mu_1,2,\gamma}$, as we observed that two isolated muons are well-separated from the photon. Additionally, we implemented a complementary selection based on the ratio $E_\gamma/M_{\mu_1\mu_2}$ to further reduce the contribution from $\mu^+\mu^- \rightarrow \gamma\mu^+\mu^-$. Specifically, we set the ratio $E_\gamma/M_{\mu_1\mu_2} > 29$ which effectively reduced background events while retaining most of the signal events. Since the average position of the $M_{\mu_1\mu_2}$ distribution for the $\mu^+\mu^- \rightarrow \gamma\mu^+\mu^-$ process is considerably wider than that of the signal, the μ ALP mass window could further reduce the number of background events. Finally, we consider a benchmark integrated luminosity of a muon collider with $\mathcal{L} = 1000$ fb $^{-1}$ to our analysis. After all of these event selections in Table. IV, we find the signal significance can reach $Z = 6.379$.

For the second signal signature, possible SM backgrounds come from $\gamma b\bar{b}$ and $\gamma c\bar{c}$ where the heavy flavor mesons generated from c and b jets can decay into a collimated muon pair and mimic the J_μ from the signal. The pre-selection cuts ($P_T^\mu > 5$ GeV, $|\eta_\mu| < 2.5$) at parton-level have been used for signal and background processes. We still choose the signal benchmark point as $m_a = 5$ GeV and $c_\mu^A/\Lambda = 10$ TeV $^{-1}$. Applying the C/A jet clustering algorithm for J_μ with a cone size $R = 0.1$, we implement event selection criteria to isolate the signal and suppress background events as specified below :

- (1) $N(\mu) \geq 2$ with $P_T^{\mu_{1,2}} > 5$ GeV, $|\eta_{\mu_{1,2}}| < 2.5$,
- (2) $N(J_\mu) = 1$ and $P_T^{J_\mu} > 750$ GeV, $|\eta_{J_\mu}| < 1.5$,

- (3) $E_\gamma > 1400$ GeV and $|\eta_\gamma| < 1.0$,
- (4) $|M_{J_\mu} - m_a| < 3.0$ GeV,
- (5) $100 < E_\gamma/M_{J_\mu} < 400$.

The reasons for implementing these event selection criteria are similar to that described earlier, and will not be repeated here again. A cut-flow table detailing the signal and backgrounds for each event selection is presented in Table. V with some relevant kinematic distributions shown in Fig. 10 of Appendix A. Employing all the event selections listed in Table. III, we find that the signal significance can achieve a value of $Z = 20.10$ with $\mathcal{L} = 1000$ fb⁻¹.

cut flow in σ [fb]	signal	$\mu^+\mu^- \rightarrow \mu^+\mu^-\mu^+\mu^-$
Generator	1.06×10^{-3}	2.82
cut-(1)	1.03×10^{-3}	1.26
cut-(2)	6.53×10^{-4}	3.26×10^{-1}
cut-(3)	4.74×10^{-4}	1.59×10^{-1}
cut-(4)	4.35×10^{-4}	5.80×10^{-2}
cut-(5)	3.43×10^{-4}	3.67×10^{-3}

TABLE VI: Similar to Table. IV, but for the $\mu^+\mu^- \rightarrow \mu^+\mu^-a$ channel and relevant SM backgrounds with the signature of four isolated muons.

In the subsequent section, we analyze the process $\mu^+\mu^- \rightarrow \mu^+\mu^-a$ (include $\mu^+\mu^- \rightarrow Za \rightarrow (\mu^+\mu^-)a$) using the same method as Sec. IV A. The signal signatures are classified into two categories : (1) four isolated muons for $m_a \gtrsim 15$ GeV, and (2) a J_μ plus two isolated muons for $m_a \lesssim 15$ GeV. To investigate the first signal signature, we consider the relevant SM background: $\mu^+\mu^- \rightarrow \mu^+\mu^-\mu^+\mu^-$ and choose the same signal benchmark point $m_a = 50$ GeV with $c_\mu^A/\Lambda = 10$ TeV⁻¹ to display the signal features. The following event selections to identify the signal signature and suppress background events are required :

- (1) $N(\mu) \geq 4$ with $P_T^{\mu_{1,2,3,4}} > 5$ GeV, $|\eta_{\mu_{1,2,3,4}}| < 2.5$,
- (2) $P_T^{\mu_1} > 200$ GeV, $P_T^{\mu_{2,3}} > 100$ GeV, $|\eta_{\mu_1}| < 2.0$ and $|\eta_{\mu_4}| < 1.5$,

- (3) $\Delta\phi_{\mu_2,\mu_4} > 0.5$ and $\Delta\phi_{\mu_3,\mu_4} > 1$,
- (4) $P_T^{\mu_4}/M_{\mu_1\mu_4} > 0.05$,
- (5) $|M_{\mu_1\mu_4} - m_a| < 5.0$ GeV.

The cut-flow table including the signal and the background for each event selection is listed in Table. VI and some kinematic distributions are shown in Fig. 11 of Appendix A.

Four isolated muons with $P_T^\mu > 5$ GeV and $|\eta_\mu| < 2.5$ are applied as a trigger criteria. We observed that $P_T^{\mu_1}$, $P_T^{\mu_2}$ and $P_T^{\mu_3}$ of the signal are more energetic than that of the background. On the other hand, μ_1 and μ_4 from the signal are distributed in the central regions relative to that from the background which μ_1 and μ_4 are mainly generated by the initial muons with the forward and backward directions. Therefore, we choose the cut-(2) in the above to select candidate events. We have checked all combinations of four muons in the final state to reconstruct a pair of muons which comes from the μ ALP decay and found the pair of μ_1 and μ_4 is most likely to reconstruct the mass of μ ALP. To reduce background events, we apply the event selections based on $\Delta\phi_{\mu_2,4}$ and $\Delta\phi_{\mu_3,4}$. We observe that the muons produced by the decay of μ ALPs in the signal are well-separated from μ_2 and μ_3 . Furthermore, we incorporate an additional selection criterion involving the ratio $P_T^{\mu_4}/M_{\mu_1\mu_4}$ to further suppress the contribution from $\mu^+\mu^- \rightarrow \mu^+\mu^-\mu^+\mu^-$. Specifically, we set the ratio $P_T^{\mu_4}/M_{\mu_1\mu_4} > 0.05$, which effectively reduced background events while retaining the majority of signal events. Since the $M_{\mu_1\mu_4}$ distribution for the $\mu^+\mu^- \rightarrow \mu^+\mu^-\mu^+\mu^-$ process is almost concentrated in the region larger than 85 GeV, the μ ALP mass window could further reduce the number of background events. Finally, after all of these event selections in Table. VI, we find the signal significance can reach $Z = 10.44$ for $\mathcal{L} = 1000$ fb $^{-1}$ in our analysis.

For the second signal signature, possible SM backgrounds come from $\mu^+\mu^-c\bar{c}$ and $\mu^+\mu^-b\bar{b}$. The pre-selection cuts ($P_T^\mu > 5$ GeV, $|\eta_\mu| < 2.5$) at parton-level have been used for signal and background process. We still choose the signal benchmark point as $m_a = 5$ GeV and $c_\mu^A/\Lambda = 10$ TeV $^{-1}$. Applying the same C/A jet clustering algorithm for a J_μ with a cone size $R = 0.1$, we set up event selections to pick up the signal and suppress background events as specified below :

- (1) $N(\mu) \geq 4$ with $P_T^{\mu_{1,2,3,4}} > 5$ GeV, $|\eta_{\mu_{1,2,3,4}}| < 2.5$,
- (2) $P_T^{\mu_{2,3}} > 100$ GeV, $|\eta_{\mu_{2,3}}| < 2.0$,

cut flow in σ [fb]	signal	$\mu^+\mu^-c\bar{c}$	$\mu^+\mu^-b\bar{b}$
Generator	1.26×10^{-3}	52.94	90.18
cut-(1)	1.13×10^{-3}	1.98×10^{-3}	7.01×10^{-2}
cut-(2)	7.19×10^{-4}	5.82×10^{-4}	2.12×10^{-2}
cut-(3)	6.63×10^{-4}	2.65×10^{-4}	1.52×10^{-2}
cut-(4)	6.61×10^{-4}	1.06×10^{-4}	1.25×10^{-2}
cut-(5)	6.03×10^{-4}	0	8.21×10^{-3}
cut-(6)	5.39×10^{-4}	0	5.41×10^{-4}

TABLE VII: Similar to Table. V, but for the $\mu^+\mu^- \rightarrow \mu^+\mu^-a$ channel and relevant SM backgrounds with the signature of a J_μ candidate plus two isolated muons.

- (3) $N(J_\mu) = 1$ with $300 < P_T^{J_\mu} < 1400$ GeV, $|\eta_{J_\mu}| < 1.6$,
- (4) $\Delta\phi_{J_\mu, \mu_2} > 4.5$ and $1.0 < \Delta\phi_{\mu_2, \mu_3} < 5.0$,
- (5) $P_T^{\mu_2}/M_{J_\mu} < 500$,
- (6) $|M_{J_\mu} - m_a| < 4$ GeV.

The event selection criteria have been implemented for reasons similar to those previously described and will not be reiterated here. The cut-flow table, which includes both signal and background events for each selection, is presented in Table. VII, while the corresponding kinematic distributions can be found in Fig. 12 of Appendix A. Upon applying all of the event selections outlined in Table. VII, we observe a significant signal significance of $Z = 19.86$ for our benchmark point with $\mathcal{L} = 1000 \text{ fb}^{-1}$.

C. Main results and existing bounds

The study of signal benchmark points is extended to a wide range of m_a by employing the search strategies outlined in Sec. IV A and Sec. IV B, resulting in the identification of possible future bounds within 95% confidence level (CL) ($Z = 1.96$). To conservatively demonstrate the signal significance of the case without the survival background event after all event selections or the case of background-free assumption, a minimum of 10 signal

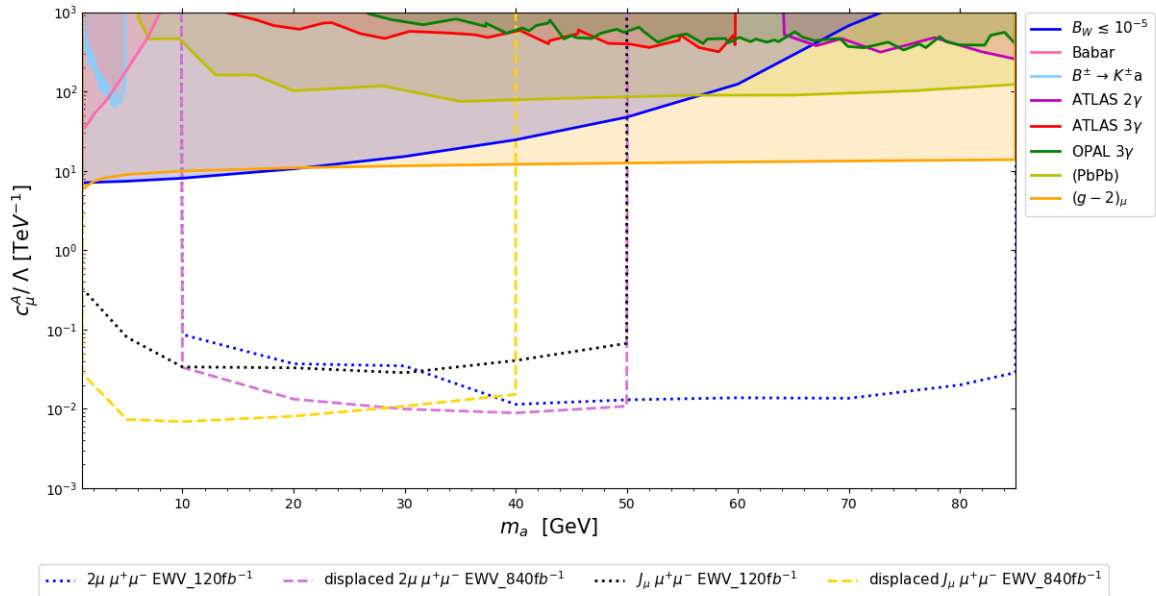


FIG. 5: The future bounds on c_μ^A/Λ of GeV-scale μ ALPs in the **EWV** scenario from the muon collider with $\mathcal{L} = 120 \text{ fb}^{-1}$ and $\mathcal{L} = 840 \text{ fb}^{-1}$ within 95% CL or 10 survival events for background-free cases (dotted lines for the μ ALP prompt decay and dashed lines for the μ ALP as a LLP) as well as existing bounds (bulk regions). Here we label "2 μ " and " J_μ " to identify two kinds of signatures at a muon collider. $\mathcal{B}_W \lesssim 10^{-5}$ represents

$\mathcal{B}(W^\pm \rightarrow \mu^\pm \nu_\mu a) < 10^{-5}$ [50] (blue bulk). For light μ ALPs, BaBar [49] (hotpink bulk), $B^\pm \rightarrow K^\pm a \rightarrow K^\pm(\gamma\gamma)$ [83] (lightskyblue bulk) are considered. Some other collider bounds are in order : ATLAS 2 γ [32, 33, 35] (magenta bulk), ATLAS 3 γ [34, 35] (red bulk), OPAL 3 γ [30, 35] (green bulk), ATLAS/CMS (PbPb) [84] (yellow bulk). Finally, the bound from $(g-2)_\mu$ [85] is labeled as orange bulk.

events is required to be present, and only signal efficiency larger than 10% is considered in the analysis. Our study is restricted to $1 \text{ GeV} \leq m_a \lesssim M_W$ for μ ALPs below the electroweak scale. We first summarize our results in Fig. 5 for searching the $\mu^+\mu^- \rightarrow \nu_\mu a \bar{\nu}_\mu$ channel in the **EWV** scenario. The dotted lines are used for the case of prompt μ ALPs decay ($\gamma\beta c\tau_a < 1 \text{ mm}$) at a muon collider with $\mathcal{L} = 120 \text{ fb}^{-1}$. Note the lower bound of m_a comes from technical issues of J_μ analysis. When $m_a < 1 \text{ GeV}$, the μ ALP mass window selection is no longer powerful to distinguish the signal from backgrounds. On the other hand, since the event selections for two isolated muons plus \cancel{E} at the muon collider are sensitive to the values of m_a , event selections are dynamically optimized for different m_a to suit each case as

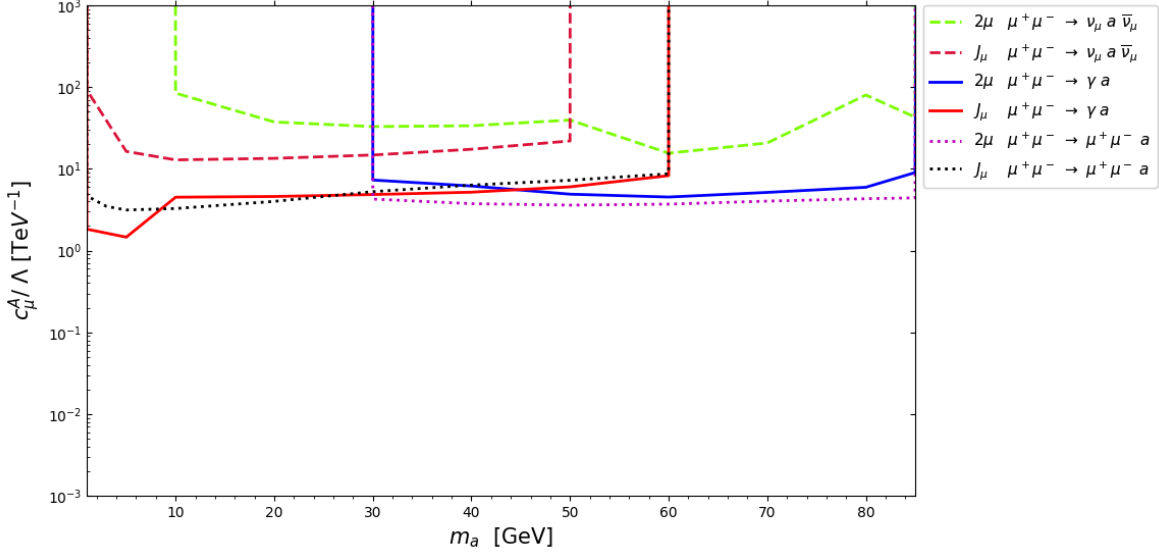


FIG. 6: The future bounds on c_μ^A/Λ of GeV-scale μ ALPs from the muon collider in the **EWP** scenario with $\mathcal{L} = 1000 \text{ fb}^{-1}$ within 95% CL or 10 survival events for background-free cases. Only the bounds from the μ ALP prompt decay are considered (dashed lines for $\mu^+\mu^- \rightarrow \nu_\mu a \bar{\nu}_\mu$, solid lines for $\mu^+\mu^- \rightarrow \gamma a$ as well as dotted lines for $\mu^+\mu^- \rightarrow \mu^+\mu^- a$). The labels of "2 μ " and " J_μ " are the same as Fig. 5.

shown in Table. VIII. The case of prompt decay of μ ALPs with two isolated muons at the muon collider yields a background-free scenario when $m_a \lesssim 30 \text{ GeV}$, causing a cusp point at $m_a = 30 \text{ GeV}$ in Fig. 5. Similarly, for the prompt decay of μ ALPs with a J_μ at the muon collider, SM background events can only survive after all event selections when $m_a = 10 \text{ GeV}$, resulting in a cusp point at $m_a = 10 \text{ GeV}$ in Fig. 5.

For μ ALPs as the LLPs, we first consider the physical size in radius of proposed detectors for muon colliders [86]. Some relevant detector parameters for the inner and outer radius of the vertex detector, ECAL, HCAL and muon system are summed up as follows : (1) $3.0 \leq R_{\text{vertex}} \leq 10.4 \text{ cm}$, (2) $150.0 \leq R_{\text{ECAL}} \leq 170.2 \text{ cm}$, (3) $174.0 \leq R_{\text{HCAL}} \leq 333.0 \text{ cm}$, (4) $446.1 \leq R_{\text{muon}} \leq 645.0 \text{ cm}$. Therefore, we simply consider the μ ALP lab frame decay length within $10^{-3} \leq \gamma\beta c\tau_a \leq 6.4 \text{ m}$ as a detectable LLP with a muon pair displaced vertex and a displaced J_μ signatures at a muon collider. We assume that both a muon pair displaced vertex and a displaced J_μ signatures at muon colliders are background-free after the trigger and μ ALP mass window selection implementation, as described in the previous text. The analysis of a muon pair displaced vertex and a displaced J_μ signatures at the muon collider

is carried out using an integrated luminosity of $\mathcal{L} = 840 \text{ fb}^{-1}$, respectively. The results of the LLP study for searching the $\mu^+\mu^- \rightarrow \nu_\mu a \bar{\nu}_\mu$ channel in the **EWV** scenario are summarized in Fig. 5 with the dashed lines. The signal efficiency of the two isolated muon signature decreases when $m_a \lesssim 30 \text{ GeV}$ because these two muons become too close to each other and cannot pass the muon isolation criterion. Similarly, grouping two muons inside a J_μ candidate is challenging for $m_a \gtrsim 10 \text{ GeV}$ at the muon collider. Therefore, the analysis of signatures with two isolated muons and a J_μ complement each other for μALP searches in the middle m_a range.

Some existing bounds are also shown in Fig. 5 for the comparison. First of all, according to the interaction in Eq. (1), there is a new W boson exotic decay channel, $W^+ \rightarrow \mu^+ \nu_\mu a$. The precision measurements of W boson width ($\Gamma_W = 2.085 \pm 0.042 \text{ GeV}$ [87]) can indirectly test μALP with $m_a < M_W$ in the **EWV** scenario. Here we conservatively require the branching ratio of $W^+ \rightarrow \mu^+ \nu_\mu a$ to be less than 10^{-5} [50] and mark it as the blue bulk in Fig. 5. For lighter μALPs ($m_a \lesssim 5 \text{ GeV}$), searching for four muons in the final state [83] (hotpink bulk) and $B^\pm \rightarrow K^\pm a$ (light skyblue bulk) by BaBar experiments can already constrain some parameter space in the upper-left corner. For heavier μALPs ($m_a > 5 \text{ GeV}$), the ATLAS 2γ [32, 33, 35] (magenta bulk), ATLAS 3γ [34, 35] (red bulk), OPAL 3γ [30, 35] (green bulk), ATLAS/CMS (PbPb) [84] (yellow bulk) can already exclude some parameter space with $c_\mu^A/\Lambda \gtrsim 10^2 \text{ TeV}^{-1}$. On the other hand, the precision measurements of muon magnetic moment can also provide constraints for μALPs . The combined measurement from Fermilab and Brookhaven is reported as $a_\mu^{\text{EXP}} = 116,592,061(41) \times 10^{-11}$ [88] and if we consider the lattice calculation for hadronic vacuum polarization (HVP), the SM prediction value change to $a_\mu^{\text{SM}} = 116,591,954(55) \times 10^{-11}$ [89]. In this situation, the deviation of $(g-2)_\mu$ is reported as $\Delta a_\mu = a_\mu^{\text{EXP}} - a_\mu^{\text{SM}} = 107(69) \times 10^{-11}$ and we consider the Δa_μ observation within 2σ for μALPs in this work. The one-loop contributions from light μALPs to $(g-2)_\mu$ is negative and can be written as²

$$\Delta a_\mu^{1\text{-loop}} = \Delta a_\mu^{\mu a \mu} + \Delta a_\mu^{\mu a \gamma} \quad , \quad (6)$$

where the first term comes from the μ - a - μ loop and the second term comes from the μ - a - γ

² The one-loop contribution from $aZ\gamma$ interaction and the two-loop contribution from aW^+W^- as well as the two-loop light-by-light contribution are much suppressed compared with Eq. (6). Hence, we can safely ignore their effects here.

loop as shown in Ref. [85] for the following form,

$$\Delta a_{\mu}^{\mu a \mu} = - \left(\frac{c_{\mu}^A m_{\mu}}{\Lambda} \right)^2 \frac{r}{8\pi^2} \int_0^1 dx \frac{x^3}{1-x+rx^2} , \quad (7)$$

$$\Delta a_{\mu}^{\mu a \gamma} = - \frac{\alpha_{\text{em}}}{4\pi^3} \left(\frac{c_{\mu}^A m_{\mu}}{\Lambda} \right)^2 \times \int_0^1 dx \left[(1-x) \left(\ln \frac{\Lambda_{\text{loop}}^2}{\Delta^2} - \frac{1}{2} \right) - 3r \left\{ x^2 \ln \left(\frac{rx^2 + (1-x)}{rx^2} \right) \right\} \right] . \quad (8)$$

Here $r = m_{\mu}^2/m_a^2$, $\Delta^2 = m_{\mu}^2 x^2 + m_a^2(1-x)$ and Λ_{loop} is the cut-off scale of the loop integration which is taken to be 1 TeV here. The strongest constraint among all the above ones is from $(g-2)_{\mu}$ [85] (orange bulk), with $c_{\mu}^A/\Lambda \gtrsim 10 \text{ TeV}^{-1}$ and extending to a wide range of m_a . It is important to note that all the above bounds have been rescaled according to our definition of ALP-muon interactions in Eq. (2) and μ ALP decay branching ratios in Fig. 1. However, some of the other bounds such as OPAL 2γ [30, 35], Belle II [90], and LHCb [91], are so weak that we have not included them here. In comparison to these existing bounds, our proposals to search for μ ALPs via $\mu^+ \mu^- \rightarrow \nu_{\mu} a \bar{\nu}_{\mu}$ at muon colliders are still attractive. Furthermore, the possible future bounds of c_{μ}^A/Λ can reach less than $0.01 - 0.1 \text{ TeV}^{-1}$, which open new doors to explore m_a in the **EWV** scenario below the electroweak scale.

In addition, as we have discussed in Sec. III, in the **EWV** scenario, cross sections are more than six orders of magnitude larger than those in the **EWP** scenario for $\mu^+ \mu^- \rightarrow \nu_{\mu} a \bar{\nu}_{\mu}$ processes in Fig. 3. Therefore, future bounds from this channel in the **EWP** scenario are as small as existing bounds. Additionally, almost the entire cross-section comes from \mathbf{aVV}' interaction in the **EWP** scenario at the muon collider. Comparing the **EWP** scenario with the **EWV** one, the longitudinal momentum (P_z) becomes larger than the transverse momentum (P_T) for two isolated muon pair, because the dominant contribution in the signal process is $\mu^+ \mu^- \rightarrow Za \rightarrow (\nu \bar{\nu})(\mu^+ \mu^-)$ instead of the one from the four-point interaction. When $m_a \gtrsim 30 \text{ GeV}$, the total energy will be roughly equally divided into Z and the ALP, resulting in large changes in some kinematic distributions. In order for comparison, we used the same event selections for both **EWV** and **EWP** scenarios. Most of the signal efficiencies are below 10% in the **EWP** scenario because the condition $P_T^{\mu_1} > 200 \text{ GeV}$ is too stringent in this situation. Meanwhile, the efficiency of the signal is also very sensitive to $E/M_{\mu_1 \mu_2}$. Thus, as we can expect, the distributions of two isolated muons in **EWP** scenario are distinct from the ones in the **EWV** scenario. Eventually, the **EWP** signal efficiency

is about 10% to 40% less than that of the **EWV** one. At the same time, we explore the potential results of searching for μ ALPs in different channels with $\mathcal{L} = 1000 \text{ fb}^{-1}$. Except for $\mu^+\mu^- \rightarrow \nu_\mu a \bar{\nu}_\mu$, we also include $\mu^+\mu^- \rightarrow \gamma a$, and $\mu^+\mu^- \rightarrow \mu^+\mu^- a$ in the **EWP** scenario. Due to different generation mechanisms among these channels, the coverage range of the interval of m_a may vary. The case of prompt decay of μ ALPs with two isolated muons in the $\mu^+\mu^- \rightarrow \gamma a$ channel yields a background-free scenario when $m_a \gtrsim 10 \text{ GeV}$, causing a cusp point at $m_a = 10 \text{ GeV}$ in Fig. 6. The case of prompt decay of μ ALPs with four isolated muons in the $\mu^+\mu^- \rightarrow \mu^+\mu^- a$ channel causes a cusp point at $m_a = 5 \text{ GeV}$ in Fig. 6. Finally, we find that a photon plus a μ ALP channel shows the best potential for searching for μ ALPs in the **EWP** scenario. The possible future bounds on c_μ^A/Λ can reach values less than $1 - 10 \text{ TeV}^{-1}$, which is only slightly greater than existing bounds.

V. CONCLUSIONS

Axion-like particles (ALPs) are pseudo-Nambu Goldstone bosons that exist beyond the standard model (SM). In the effective field theory framework, ALPs are allowed to have masses ranging from nearly massless to the electroweak scale or higher, and their couplings with SM particles can be investigated independently. Therefore, it is crucial to search for ALPs with various mass ranges and interaction types. This study focuses on exploring the search for the GeV-scale muonphilic ALPs (μ ALPs), a specific type of ALPs that interact predominantly with muons, at a muon collider.

Producing GeV-scale μ ALPs is challenging due to their suppressed production cross sections, which are proportional to the square of the muon mass. Hence, a new proposal is necessary to produce them effectively at high-energy colliders. This study proposes four production channels that can be used to search for μ ALPs at muon colliders: $\mu^+\mu^- \rightarrow \nu_\mu a \bar{\nu}_\mu$, $\mu^+\mu^- \rightarrow \gamma a$, $\mu^+\mu^- \rightarrow Z a$ and $\mu^+\mu^- \rightarrow \mu^+\mu^- a$ which rely on a four-point interaction, W - μ - ν_μ - a , and/or interactions arising from the chiral anomaly that do not depend on the muon mass. It is noteworthy that in the electroweak violating (**EWV**) scenario, the cross section of the $\mu^+\mu^- \rightarrow \nu_\mu a \bar{\nu}_\mu$ process is six to seven orders of magnitude larger than that of other channels, as shown in Table. VIII, due to the energy enhancement behavior resulting from the W - μ - ν_μ - a interaction. However, in the electroweak preserving (**EWP**) scenario, the four-point interaction disappears, and the $\mu^+\mu^- \rightarrow \gamma a$ channel has the largest cross section.

In the search for GeV-scale μ ALPs at a muon collider, different search strategies are employed for the **EWV** and **EWP** scenarios. We focus on the production channels $\mu^+\mu^- \rightarrow \nu_\mu a \bar{\nu}_\mu$ in the **EWV** scenario, and $\mu^+\mu^- \rightarrow \gamma a$ and $\mu^+\mu^- \rightarrow \mu^+\mu^- a$ in the **EWP** scenario. On the other hand, the GeV-scale μ ALP mainly decays into a pair of muons. When the light μ ALP is highly boosted and produced at a muon collider, these two muons are too collimated to pass standard muon isolation criteria and form a novel object called a muon-jet, J_μ . Therefore, this study explores two types of signatures : (1) two isolated muons plus other parts, and (2) a J_μ plus other parts. These two signature types are complementary in the search for the GeV-scale μ ALP. The signature of J_μ can cover low-mass μ ALP detection range well, and the signature of two isolated muons can cover high-mass μ ALP detection range. After a comprehensive signal-to-background analysis for these two kind of signatures at a muon collider, future bounds for c_μ^A/Λ are shown to be more than three orders of magnitude stronger than existing bounds for μ ALPs with $1 \text{ GeV} \leq m_a \lesssim M_W$ at integrated luminosity of $\mathcal{L} = 120 \text{ fb}^{-1}$ for the prompt μ ALP decay and $\mathcal{L} = 840 \text{ fb}^{-1}$ for the μ ALP as a long-lived particle in the **EWV** scenario, as illustrated in Fig. 5. However, future bounds for c_μ^A/Λ of μ ALPs with $1 \text{ GeV} \leq m_a \lesssim M_W$ are shown to be barely exceed existing bounds in the **EWP** scenario, even with an integrated luminosity of $\mathcal{L} = 1000 \text{ fb}^{-1}$, as illustrated in Fig. 6. Overall, this study provides important insights into the potential to explore GeV-scale μ ALPs. Such efforts will motivate experimentalists to pursue μ ALP searches at future muon colliders.

Appendix A: Some kinematic distributions and supplemental information

In this Appendix, we choose some representative kinematic distributions for both signals and backgrounds at at a muon collider in the following :

- For the signature of two isolated muons plus \cancel{E} at at a $\mu^+\mu^-$ collider, $P_T^{\mu_1}$, η_{μ_1} , \cancel{E} , $M_{\mu_1\mu_2}$, $\Delta\phi_{\mu_1, \cancel{E}}$ and $\Delta\phi_{\mu_2, \cancel{E}}$ distributions for $m_a = 50 \text{ GeV}$ with $c_\mu^A/\Lambda = 0.1 \text{ TeV}^{-1}$ are shown in Fig. 7.
- For the signature of a J_μ plus \cancel{E} at a $\mu^+\mu^-$ collider, $P_T^{J_\mu}$, η_{J_μ} , \cancel{E} and M_{J_μ} distributions for $m_a = 5 \text{ GeV}$ with $c_\mu^A/\Lambda = 0.1 \text{ TeV}^{-1}$ are shown in Fig. 8.
- For the signature of two isolated muons plus a γ at at $\mu^+\mu^-$ colliders, $P_T^{\mu_1}$, η_{μ_1} , E_γ ,

$M_{\mu_1\mu_2}$, $\Delta\phi_{\mu_1,\gamma}$ and $E_\gamma/M_{\mu_1\mu_2}$ distributions for $m_a = 50$ GeV with $c_\mu^A/\Lambda = 10$ TeV $^{-1}$ are shown in Fig. 9.

- For the signature of a J_μ plus a γ at a $\mu^+\mu^-$ collider, $P_T^{J_\mu}$, η_{J_μ} , E_γ , η_γ , M_{J_μ} and E_γ/M_{J_μ} distributions for $m_a = 5$ GeV with $c_\mu^A/\Lambda = 10$ TeV $^{-1}$ are shown in Fig. 10.
- For the signature of four isolated muons at a $\mu^+\mu^-$ collider, $P_T^{\mu_3}$, η_{μ_2} , η_{μ_4} , $\Delta\phi_{\mu_3,\mu_4}$, $P_T^{\mu_4}/M_{\mu_1\mu_4}$ and $M_{\mu_1\mu_4}$ distributions for $m_a = 50$ GeV with $c_\mu^A/\Lambda = 10$ TeV $^{-1}$ are shown in Fig. 11.
- For the signature of two isolated muons plus a J_μ at a $\mu^+\mu^-$ collider, η_{μ_2} , η_{J_μ} , $P_T^{J_\mu}$, $\Delta\phi_{\mu_2\mu_3}$, $M_{\mu_1\mu_4}/(P_T^{\mu_1} + P_T^{\mu_4})$ and M_{J_μ} distributions for $m_a = 5$ GeV with $c_\mu^A/\Lambda = 10$ TeV $^{-1}$ are shown in Fig. 12.

On the other hand, we modify the event selections for detecting two isolated muons plus \cancel{E} with varying m_a at a muon collider (as shown in Table. VIII) to optimize the signal efficiency. Specifically, we adjust the ranges of $\eta_{\mu_{1,2}}$ and $\eta_{\cancel{E}}$ for small values of m_a , as loosening these criteria can improve signal detection while still eliminating all background events with the current selection criteria. In addition, we adjust $\cancel{E}/M_{\mu_1\mu_2}$ based on signal and background distributions since it decreases as m_a increases. Conversely, we do not optimize event selections for detecting a J_μ plus \cancel{E} with varying m_a at a muon collider since the relevant backgrounds are already unlikely to satisfy the conditions of two detectable muons in the muon spectrometer and forming an energetic J_μ in the central region. As a result, nearly all of these signals are free from background events after the cut-(3) selection in Table. III. Similarly, we fine-tune event selections for detecting two isolated muons plus a photon and four isolated muons at a muon collider for different m_a in the **EWP** scenario, as listed in Table IX and Table X.

-
- [1] R. D. Peccei and H. R. Quinn, Phys. Rev. Lett. **38**, 1440-1443 (1977) doi:10.1103/PhysRevLett.38.1440
- [2] S. Weinberg, Phys. Rev. Lett. **40**, 223-226 (1978) doi:10.1103/PhysRevLett.40.223
- [3] F. Wilczek, Phys. Rev. Lett. **40**, 279-282 (1978) doi:10.1103/PhysRevLett.40.279
- [4] J. E. Kim, Phys. Rev. Lett. **43**, 103 (1979) doi:10.1103/PhysRevLett.43.103

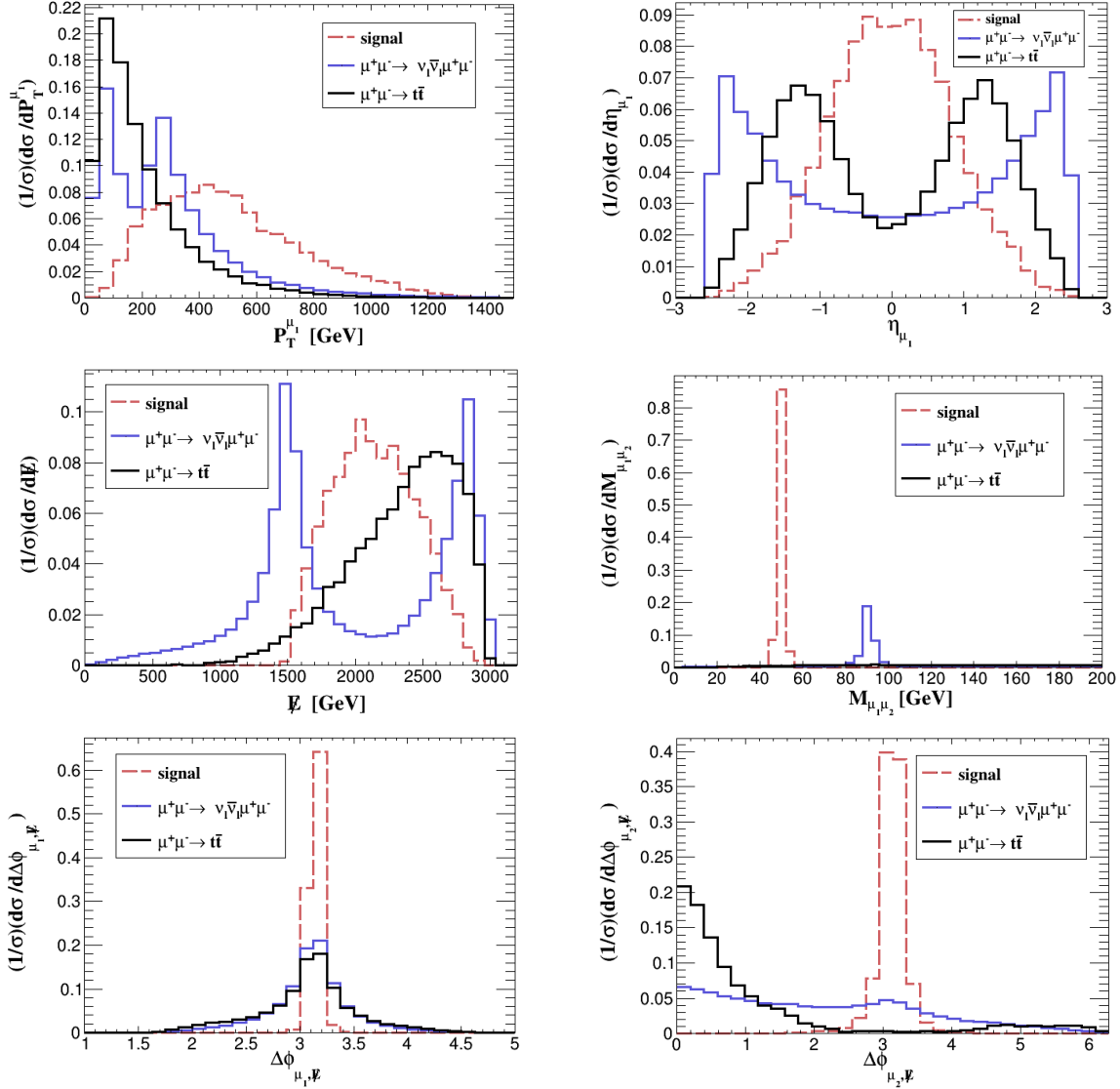


FIG. 7: Some signal and background kinematic distributions for the signature of two isolated muons plus \cancel{E} at a $\mu^+\mu^-$ collider, $P_T^{\mu_1}$, η_{μ_1} , E , $M_{\mu_1\mu_2}$, $\Delta\phi_{\mu_1,\cancel{E}}$ and $\Delta\phi_{\mu_2,\cancel{E}}$ distributions for $m_a = 50$ GeV with $c_\mu^A/\Lambda = 0.1$ TeV $^{-1}$.

- [5] J. E. Kim and G. Carosi, Rev. Mod. Phys. **82**, 557-602 (2010) [erratum: Rev. Mod. Phys. **91**, no.4, 049902 (2019)] doi:10.1103/RevModPhys.82.557 [arXiv:0807.3125 [hep-ph]].
- [6] J. Preskill, M. B. Wise and F. Wilczek, Phys. Lett. B **120**, 127-132 (1983) doi:10.1016/0370-2693(83)90637-8
- [7] L. F. Abbott and P. Sikivie, Phys. Lett. B **120**, 133-136 (1983) doi:10.1016/0370-2693(83)90638-X
- [8] M. Dine and W. Fischler, Phys. Lett. B **120**, 137-141 (1983) doi:10.1016/0370-2693(83)90639-1

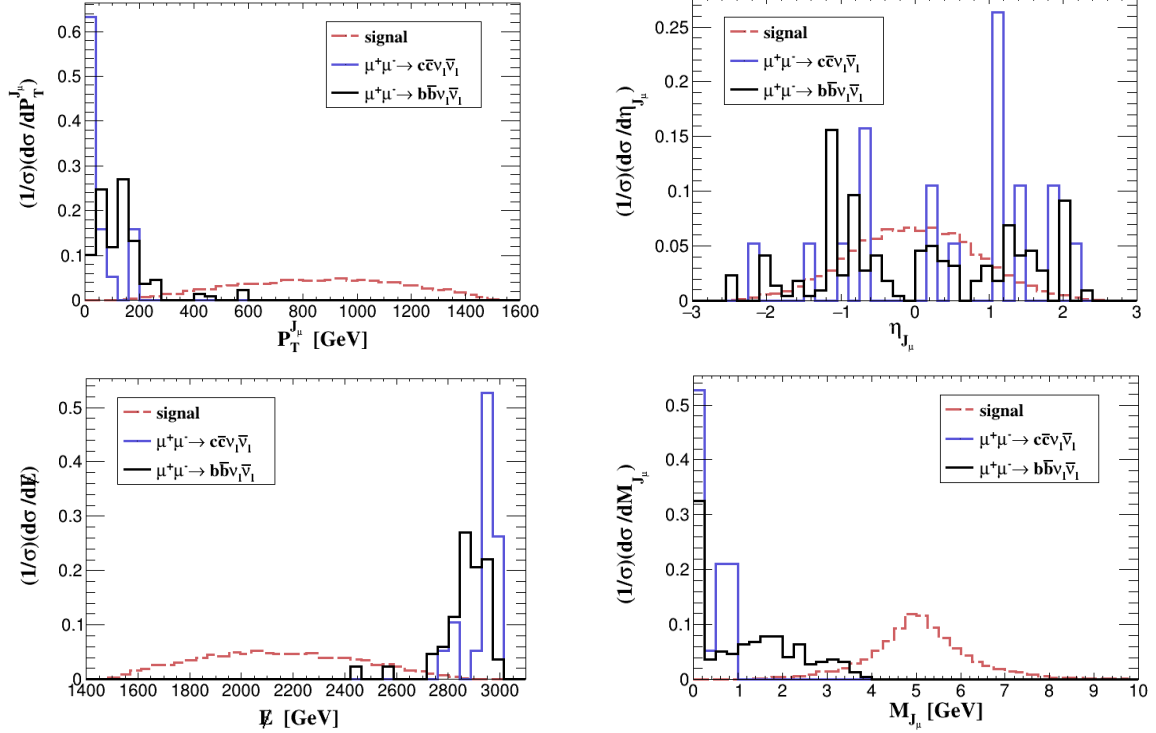


FIG. 8: Some signal and background kinematic distributions for the signature of a J_μ plus \cancel{E} at a $\mu^+\mu^-$ collider, $P_T^{J_\mu}$, η_{J_μ} , \cancel{E} and M_{J_μ} distributions for $m_a = 5$ GeV with $c_\mu^A/\Lambda = 0.1$ TeV^{-1} .

- [9] J. Bagger, E. Poppitz and L. Randall, Nucl. Phys. B **426**, 3-18 (1994) doi:10.1016/0550-3213(94)90123-6 [arXiv:hep-ph/9405345 [hep-ph]].
- [10] P. Svrcek and E. Witten, JHEP **06**, 051 (2006) doi:10.1088/1126-6708/2006/06/051 [arXiv:hep-th/0605206 [hep-th]].
- [11] A. Arvanitaki, S. Dimopoulos, S. Dubovsky, N. Kaloper and J. March-Russell, Phys. Rev. D **81**, 123530 (2010) doi:10.1103/PhysRevD.81.123530 [arXiv:0905.4720 [hep-th]].
- [12] M. Cicoli, M. Goodsell and A. Ringwald, JHEP **10**, 146 (2012) doi:10.1007/JHEP10(2012)146 [arXiv:1206.0819 [hep-th]].
- [13] L. Visinelli and S. Vagnozzi, Phys. Rev. D **99**, no.6, 063517 (2019) doi:10.1103/PhysRevD.99.063517 [arXiv:1809.06382 [hep-ph]].
- [14] S. Chang, S. Tazawa and M. Yamaguchi, Phys. Rev. D **61**, 084005 (2000) doi:10.1103/PhysRevD.61.084005 [arXiv:hep-ph/9908515 [hep-ph]].
- [15] M. Bastero-Gil, C. Beaufort and D. Santos, JCAP **10**, 048 (2021) doi:10.1088/1475-

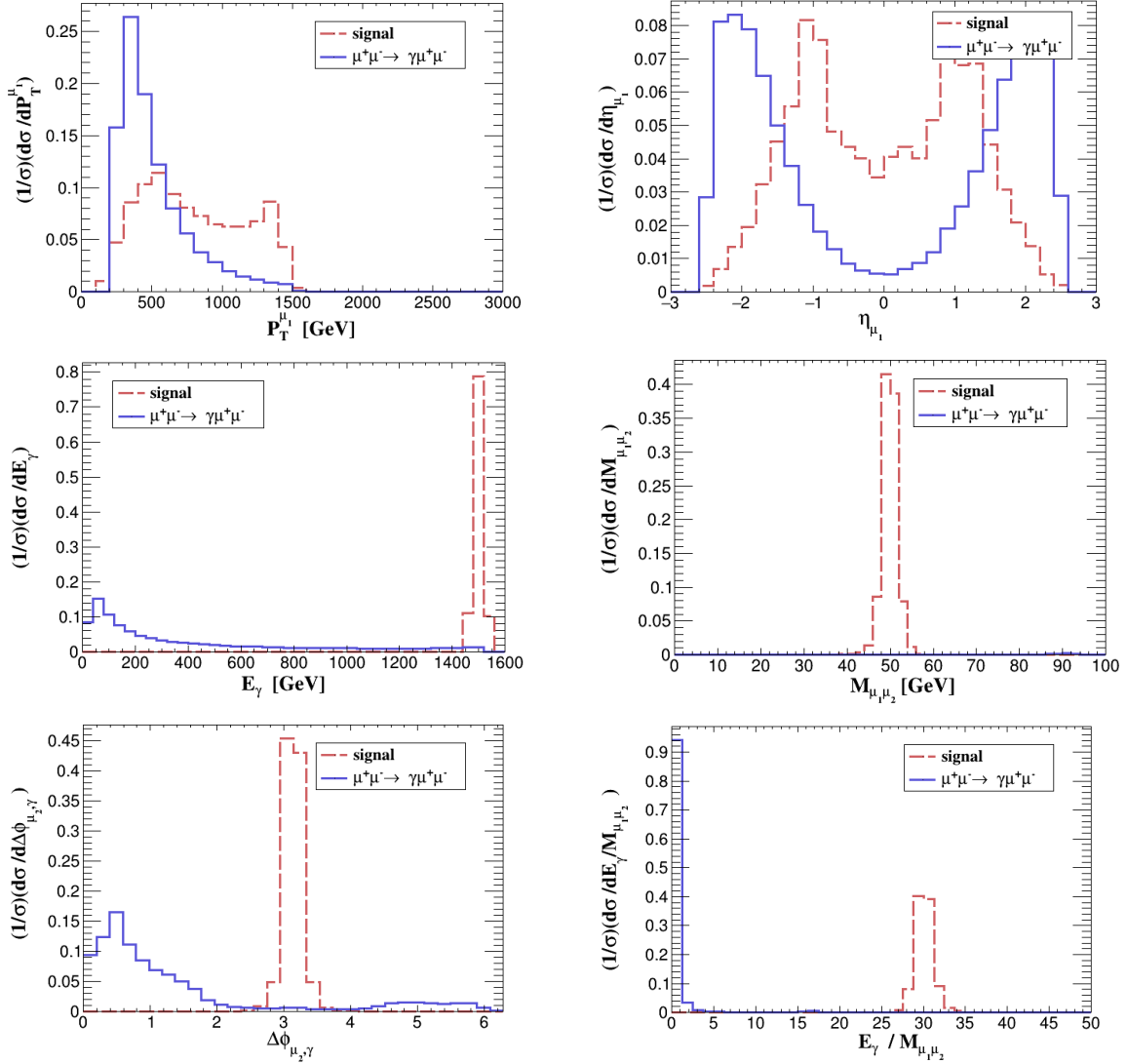


FIG. 9: Some signal and background kinematic distributions for the signature of two isolated muons plus a γ at a $\mu^+\mu^-$ collider, $P_T^{\mu_1}$, η_{μ_1} , E_γ , $M_{\mu_1\mu_2}$, $\Delta\phi_{\mu_1,\gamma}$ and $E_\gamma/M_{\mu_1\mu_2}$ distributions for $m_a = 50$ GeV with $c_\mu^A/\Lambda = 10$ TeV $^{-1}$.

7516/2021/10/048 [arXiv:2107.13337 [hep-ph]].

- [16] J. Jaeckel and A. Ringwald, Ann. Rev. Nucl. Part. Sci. **60**, 405-437 (2010) doi:10.1146/annurev.nucl.012809.104433 [arXiv:1002.0329 [hep-ph]].
- [17] P. Arias, D. Cadamuro, M. Goodsell, J. Jaeckel, J. Redondo and A. Ringwald, JCAP **06**, 013 (2012) doi:10.1088/1475-7516/2012/06/013 [arXiv:1201.5902 [hep-ph]].
- [18] A. S. Zhevlakov, D. V. Kirpichnikov and V. E. Lyubovitskij, Phys. Rev. D **106**, no.3, 035018 (2022) doi:10.1103/PhysRevD.106.035018 [arXiv:2204.09978 [hep-ph]].

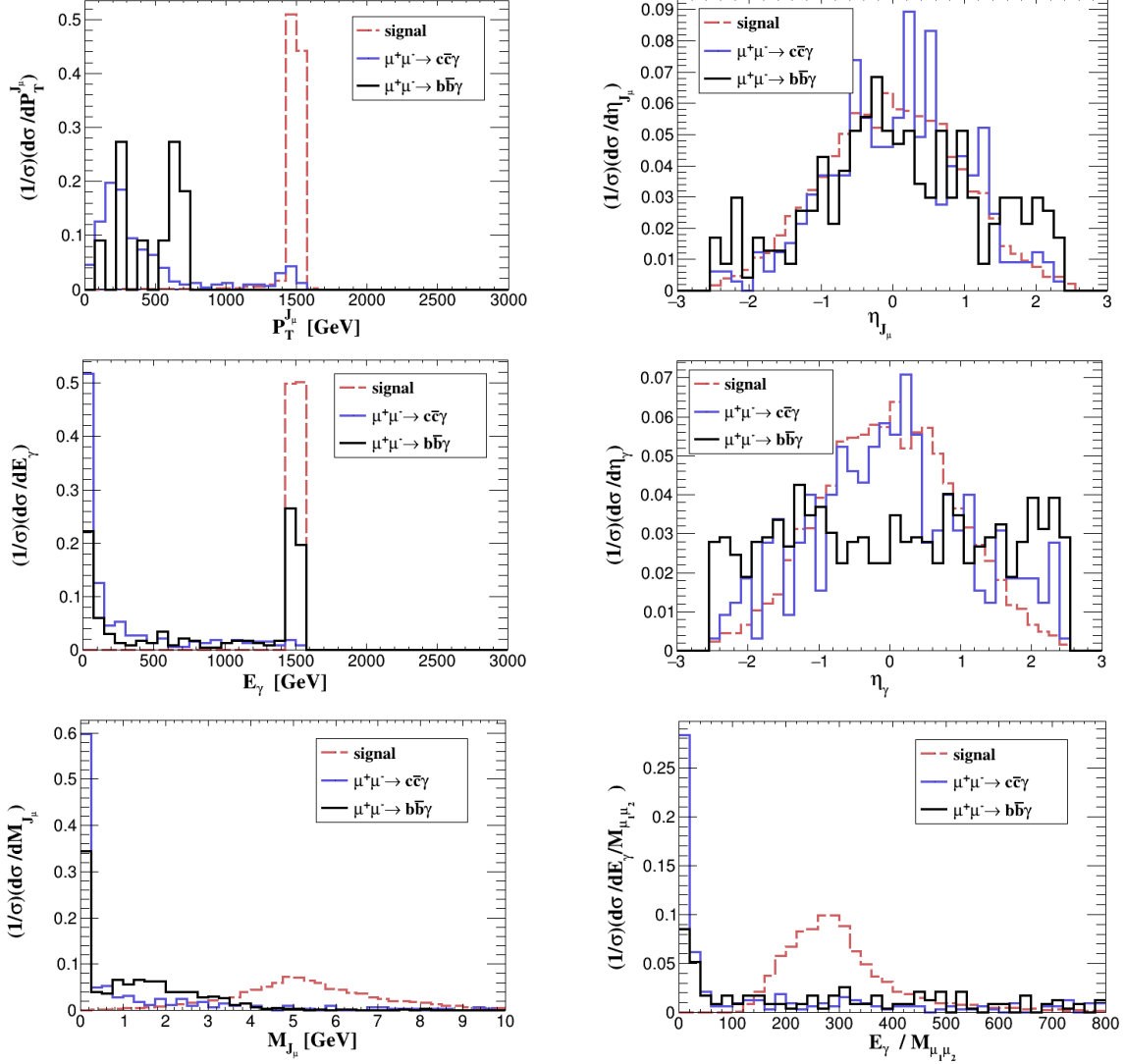


FIG. 10: Some signal and background kinematic distributions for the signature of a J_μ plus a γ at a $\mu^+\mu^-$ collider, $P_T^{J_\mu}$, η_{J_μ} , E_γ , η_γ , M_{J_μ} and E_γ/M_{J_μ} distributions for $m_a = 5$ GeV with $c_\mu^A/\Lambda = 10 \text{ TeV}^{-1}$.

- [19] A. Bharucha, F. Brümmer, N. Desai and S. Mutzel, JHEP **02**, 141 (2023) doi:10.1007/JHEP02(2023)141 [arXiv:2209.03932 [hep-ph]].
- [20] K. S. Jeong, T. H. Jung and C. S. Shin, Phys. Rev. D **101**, no.3, 035009 (2020) doi:10.1103/PhysRevD.101.035009 [arXiv:1811.03294 [hep-ph]].
- [21] S. H. Im, K. S. Jeong and Y. Lee, Phys. Rev. D **105**, no.3, 035028 (2022) doi:10.1103/PhysRevD.105.035028 [arXiv:2111.01327 [hep-ph]].
- [22] P. W. Graham, D. E. Kaplan and S. Rajendran, Phys. Rev. Lett. **115**, no.22, 221801 (2015)

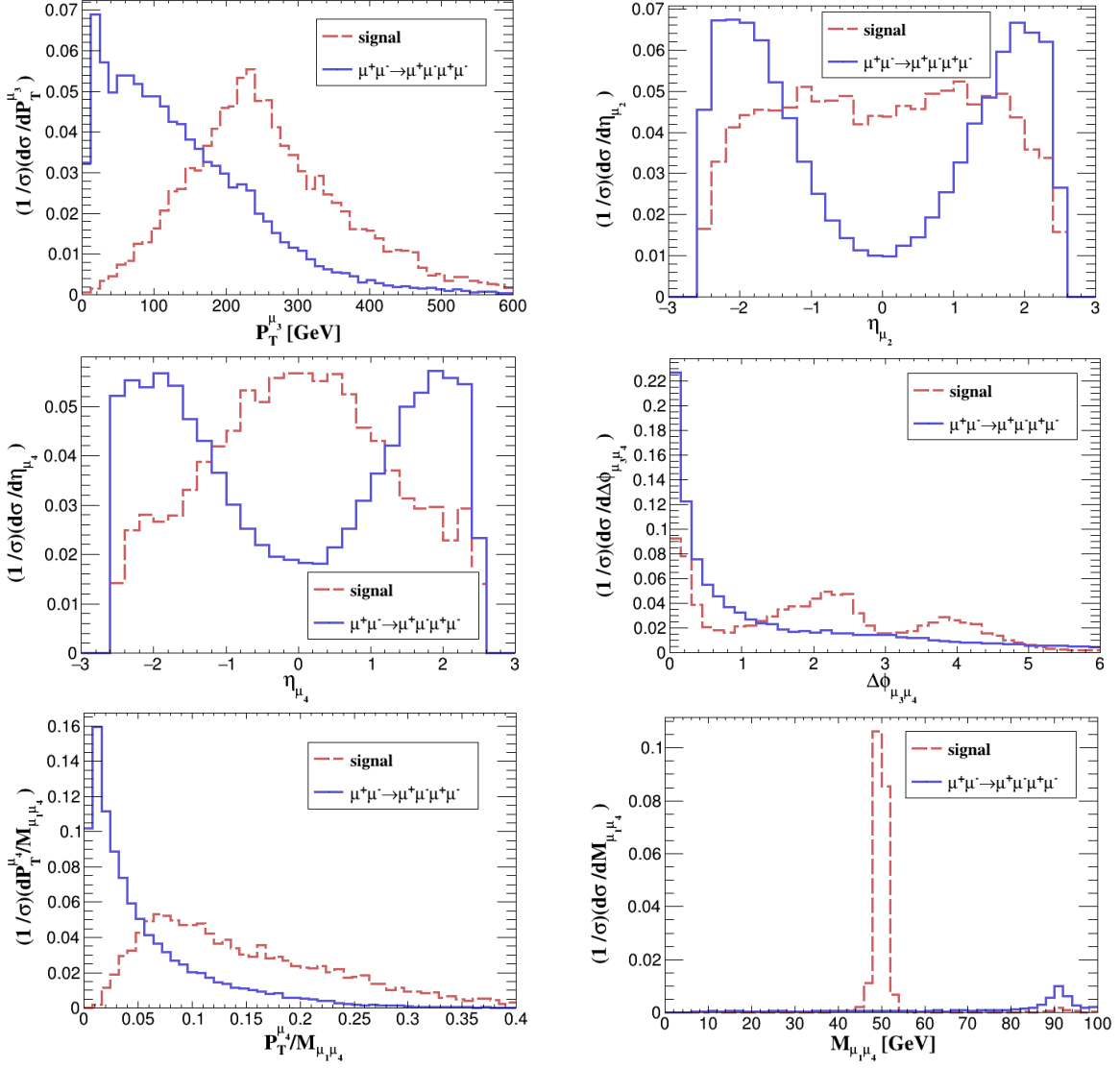


FIG. 11: Some signal and background kinematic distributions for the signature of four isolated muons at a $\mu^+\mu^-$ collider, $P_T^{\mu_3}$, η_{μ_2} , η_{μ_4} , $\Delta\phi_{\mu_3\mu_4}$, $P_T^{\mu_4}/M_{\mu_1\mu_4}$ and $M_{\mu_1\mu_4}$ distributions for $m_a = 50$ GeV with $c_\mu^A/\Lambda = 10$ TeV $^{-1}$.

doi:10.1103/PhysRevLett.115.221801 [arXiv:1504.07551 [hep-ph]].

[23] P. Sikivie, Phys. Rev. Lett. **51**, 1415-1417 (1983) [erratum: Phys. Rev. Lett. **52**, 695 (1984)] doi:10.1103/PhysRevLett.51.1415

[24] V. Anastassopoulos *et al.* [CAST], Nature Phys. **13**, 584-590 (2017) doi:10.1038/nphys4109 [arXiv:1705.02290 [hep-ex]].

[25] M. Bauer, M. Heiles, M. Neubert and A. Thamm, Eur. Phys. J. C **79**, no.1, 74 (2019) doi:10.1140/epjc/s10052-019-6587-9 [arXiv:1808.10323 [hep-ph]].

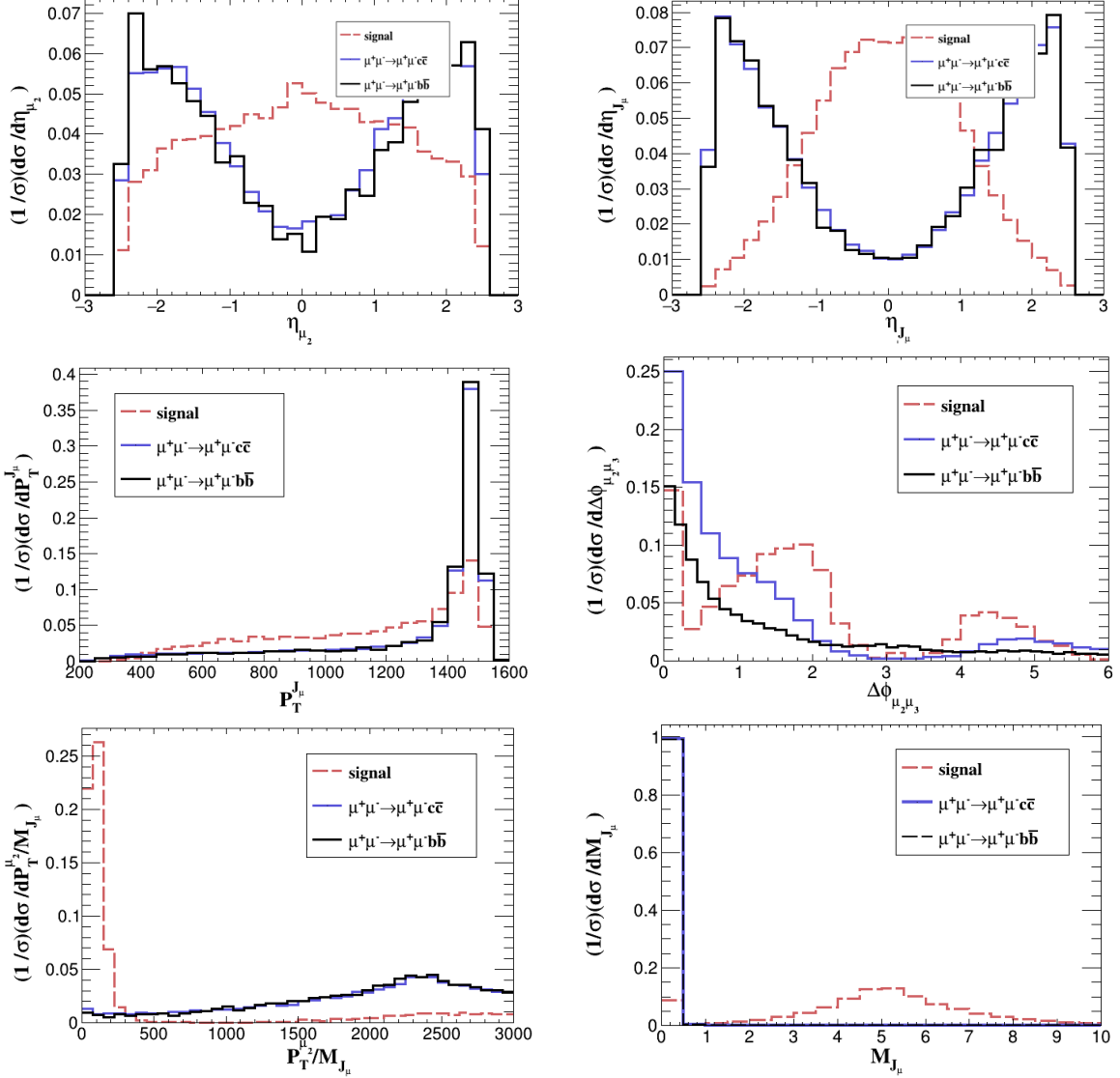


FIG. 12: Some signal and background kinematic distributions for the signature of a J_μ plus two isolated muons at a $\mu^+\mu^-$ collider, η_{μ_2} , η_{J_μ} , $P_T^{J_\mu}$, $\Delta\phi_{\mu_2\mu_3}$, $M_{\mu_1\mu_4}/(P_T^{\mu_1} + P_T^{\mu_4})$ and M_{J_μ} distributions for $m_a = 5$ GeV with $c_\mu^A/\Lambda = 10$ TeV $^{-1}$.

- [26] H. J. Li, Phys. Lett. B **829**, 137047 (2022) doi:10.1016/j.physletb.2022.137047 [arXiv:2203.08573 [astro-ph.HE]].
- [27] C. Eckner and F. Calore, Phys. Rev. D **106**, no.8, 083020 (2022) doi:10.1103/PhysRevD.106.083020 [arXiv:2204.12487 [astro-ph.HE]].
- [28] L. Mastrototaro, P. Carenza, M. Chianese, D. F. G. Fiorillo, G. Miele, A. Mirizzi and D. Montanino, Eur. Phys. J. C **82**, no.11, 1012 (2022) doi:10.1140/epjc/s10052-022-10979-6 [arXiv:2206.08945 [hep-ph]].

m_a [GeV]	$ \eta_{\mu_{1,2}} $	$ \eta_{\cancel{E}} $	$\cancel{E}/M_{\mu_1\mu_2}$	$\Delta M_{\mu_1\mu_2}$	$\Delta\phi_{\mu_2, \cancel{E}}$
10	< 3.0	< 3.0	> 140	same	(2.5, 3.6)
20	< 2.0	< 2.0	> 70	same	(2.7, 3.6)
30	< 1.8	< 1.9	> 50	same	same
40	< 1.6	same	> 40	same	same
60	same	same	> 22	< 1.5	same
70	same	same	> 22	< 1.5	same
80	same	same	> 20	< 2.3	(2.8, 3.5)
85	same	same	> 18	< 2.3	(2.8, 3.5)

TABLE VIII: The changes of some event selections in the **EWV** scenario with some m_a benchmark points for two isolated muons plus \cancel{E} at a muon collider where $\Delta M_{\mu_1\mu_2} \equiv |M_{\mu_1\mu_2} - m_a|$ and "same" means the same event selection as the benchmark point $m_a = 50$ GeV in the main text.

m_a [GeV]	$P_T^{\mu_2}$	$ \eta_{\mu_{1,2}} $	$ \eta_{E_\gamma} $	$E_\gamma/M_{\mu_1\mu_2}$	$\Delta M_{\mu_1\mu_2}$
30	> 300	same	< 1.8	> 46	same
40	> 400	same	same	> 35	< 1.8
60	same	< 1.2	< 1.2	> 24	< 2.2
70	same	< 1.2	< 1.2	(20, 23)	< 2.8
80	same	< 1.2	< 1.2	(17, 20)	< 3.0
85	same	< 1.2	< 1.2	(16, 19)	< 3.0

TABLE IX: Similar to Table. VIII, but for the $\mu^+\mu^- \rightarrow \gamma a$ channel.

- [29] H. J. Li and W. Chao, Phys. Rev. D **107**, no.6, 063031 (2023) doi:10.1103/PhysRevD.107.063031 [arXiv:2211.00524 [hep-ph]].
- [30] G. Abbiendi *et al.* [OPAL], Eur. Phys. J. C **26**, 331-344 (2003) doi:10.1140/epjc/s2002-01074-5 [arXiv:hep-ex/0210016 [hep-ex]].
- [31] K. Mimasu and V. Sanz, JHEP **06**, 173 (2015) doi:10.1007/JHEP06(2015)173 [arXiv:1409.4792 [hep-ph]].

m_a [GeV]	$ \eta_{\mu_1} $	$ \eta_{\mu_4} $	$\Delta\phi_{\mu_3,\mu_4}$	$P_T^{\mu_4}/M_{\mu_1\mu_4}$	$\Delta M_{\mu_1\mu_4}$
30	same	< 1.6	> 0.8	same	< 4.0
40	same	same	same	same	< 4.0
60	same	same	same	> 0.06	same
70	< 1.8	< 1.4	> 1.2	> 0.06	same
80	< 1.8	< 1.4	> 1.2	> 0.08	same
85	< 1.8	< 1.4	> 1.2	> 0.08	< 4.0

TABLE X: Similar to Table. VIII, but for the $\mu^+\mu^- \rightarrow \mu^+\mu^- a$ channel.

- [32] J. Jaeckel and M. Spannowsky, Phys. Lett. B **753**, 482-487 (2016) doi:10.1016/j.physletb.2015.12.037 [arXiv:1509.00476 [hep-ph]].
- [33] G. Aad *et al.* [ATLAS], Phys. Rev. Lett. **113**, no.17, 171801 (2014) doi:10.1103/PhysRevLett.113.171801 [arXiv:1407.6583 [hep-ex]].
- [34] G. Aad *et al.* [ATLAS], Eur. Phys. J. C **76**, no.4, 210 (2016) doi:10.1140/epjc/s10052-016-4034-8 [arXiv:1509.05051 [hep-ex]].
- [35] S. Knapen, T. Lin, H. K. Lou and T. Melia, Phys. Rev. Lett. **118**, no.17, 171801 (2017) doi:10.1103/PhysRevLett.118.171801 [arXiv:1607.06083 [hep-ph]].
- [36] R. Bollig, W. DeRocco, P. W. Graham and H. T. Janka, Phys. Rev. Lett. **125**, no.5, 051104 (2020) [erratum: Phys. Rev. Lett. **126**, no.18, 189901 (2021)] doi:10.1103/PhysRevLett.125.051104 [arXiv:2005.07141 [hep-ph]].
- [37] D. Croon, G. Elor, R. K. Leane and S. D. McDermott, JHEP **01**, 107 (2021) doi:10.1007/JHEP01(2021)107 [arXiv:2006.13942 [hep-ph]].
- [38] M. A. Buen-Abad, J. Fan, M. Reece and C. Sun, JHEP **09**, 101 (2021) doi:10.1007/JHEP09(2021)101 [arXiv:2104.03267 [hep-ph]].
- [39] S. F. Ge, X. D. Ma and P. Pasquini, Eur. Phys. J. C **81**, no.9, 787 (2021) doi:10.1140/epjc/s10052-021-09571-1 [arXiv:2104.03276 [hep-ph]].
- [40] A. Caputo, G. Raffelt and E. Vitagliano, Phys. Rev. D **105**, no.3, 035022 (2022) doi:10.1103/PhysRevD.105.035022 [arXiv:2109.03244 [hep-ph]].
- [41] K. Cheung, J. L. Kuo, P. Y. Tseng and Z. S. Wang, Phys. Rev. D **106**, no.9, 095029 (2022)

- doi:10.1103/PhysRevD.106.095029 [arXiv:2208.05111 [hep-ph]].
- [42] J. Liu, X. Ma, L. T. Wang and X. P. Wang, [arXiv:2210.09335 [hep-ph]].
- [43] L. Calibbi, Z. Huang, S. Qin, Y. Yang and X. Yin, [arXiv:2212.02818 [hep-ph]].
- [44] I. Brivio, M. B. Gavela, L. Merlo, K. Mimasu, J. M. No, R. del Rey and V. Sanz, *Eur. Phys. J. C* **77**, no.8, 572 (2017) doi:10.1140/epjc/s10052-017-5111-3 [arXiv:1701.05379 [hep-ph]].
- [45] M. Bauer, M. Neubert and A. Thamm, *JHEP* **12**, 044 (2017) doi:10.1007/JHEP12(2017)044 [arXiv:1708.00443 [hep-ph]].
- [46] J. Ebadi, S. Khatibi and M. Mohammadi Najafabadi, *Phys. Rev. D* **100**, no.1, 015016 (2019) doi:10.1103/PhysRevD.100.015016 [arXiv:1901.03061 [hep-ph]].
- [47] M. Bauer, M. Neubert, S. Renner, M. Schnubel and A. Thamm, *JHEP* **04**, 063 (2021) doi:10.1007/JHEP04(2021)063 [arXiv:2012.12272 [hep-ph]].
- [48] M. Bauer, M. Neubert, S. Renner, M. Schnubel and A. Thamm, *JHEP* **09**, 056 (2022) doi:10.1007/JHEP09(2022)056 [arXiv:2110.10698 [hep-ph]].
- [49] J. P. Lees *et al.* [BaBar], *Phys. Rev. D* **94**, no.1, 011102 (2016) doi:10.1103/PhysRevD.94.011102 [arXiv:1606.03501 [hep-ex]].
- [50] W. Altmannshofer, J. A. Dror and S. Gori, [arXiv:2209.00665 [hep-ph]].
- [51] C. T. Lu, [arXiv:2210.15648 [hep-ph]].
- [52] H. Al Ali, N. Arkani-Hamed, I. Banta, S. Benevedes, D. Buttazzo, T. Cai, J. Cheng, T. Cohen, N. Craig and M. Ekhterachian, *et al. Rept. Prog. Phys.* **85**, no.8, 084201 (2022) doi:10.1088/1361-6633/ac6678 [arXiv:2103.14043 [hep-ph]].
- [53] J. de Blas *et al.* [Muon Collider], [arXiv:2203.07261 [hep-ph]].
- [54] K. M. Black, S. Jindariani, D. Li, F. Maltoni, P. Meade, D. Stratakis, D. Acosta, R. Agarwal, K. Agashe and C. Aimè, *et al.* [arXiv:2209.01318 [hep-ex]].
- [55] K. Cheung and Z. S. Wang, *Phys. Rev. D* **103**, 116009 (2021) doi:10.1103/PhysRevD.103.116009 [arXiv:2101.10476 [hep-ph]].
- [56] U. Kaya, B. Ketenoglu, S. Sultansoy and F. Zimmermann, [arXiv:1905.05564 [physics.acc-ph]].
- [57] B. Dagli, B. Ketenoglu and S. Sultansoy, [arXiv:2206.00037 [physics.acc-ph]].
- [58] N. Arkani-Hamed and N. Weiner, *JHEP* **12**, 104 (2008) doi:10.1088/1126-6708/2008/12/104 [arXiv:0810.0714 [hep-ph]].
- [59] M. Baumgart, C. Cheung, J. T. Ruderman, L. T. Wang and I. Yavin, *JHEP* **04**, 014 (2009) doi:10.1088/1126-6708/2009/04/014 [arXiv:0901.0283 [hep-ph]].

- [60] Y. Bai and Z. Han, Phys. Rev. Lett. **103**, 051801 (2009) doi:10.1103/PhysRevLett.103.051801 [arXiv:0902.0006 [hep-ph]].
- [61] C. Cheung, J. T. Ruderman, L. T. Wang and I. Yavin, JHEP **04**, 116 (2010) doi:10.1007/JHEP04(2010)116 [arXiv:0909.0290 [hep-ph]].
- [62] A. Falkowski, J. T. Ruderman, T. Volansky and J. Zupan, JHEP **05**, 077 (2010) doi:10.1007/JHEP05(2010)077 [arXiv:1002.2952 [hep-ph]].
- [63] C. Han, D. Kim, S. Munir and M. Park, JHEP **04**, 132 (2015) doi:10.1007/JHEP04(2015)132 [arXiv:1502.03734 [hep-ph]].
- [64] E. Izaguirre and B. Shuve, Phys. Rev. D **91**, no.9, 093010 (2015) doi:10.1103/PhysRevD.91.093010 [arXiv:1504.02470 [hep-ph]].
- [65] E. Izaguirre, G. Krnjaic and B. Shuve, Phys. Rev. D **93**, no.6, 063523 (2016) doi:10.1103/PhysRevD.93.063523 [arXiv:1508.03050 [hep-ph]].
- [66] J. Chang, K. Cheung, S. C. Hsu and C. T. Lu, Phys. Rev. D **95**, no.3, 035012 (2017) doi:10.1103/PhysRevD.95.035012 [arXiv:1607.07550 [hep-ph]].
- [67] M. Kim, H. S. Lee, M. Park and M. Zhang, Phys. Rev. D **98**, no.5, 055027 (2018) doi:10.1103/PhysRevD.98.055027 [arXiv:1612.02850 [hep-ph]].
- [68] S. Dube, D. Gadkari and A. M. Thalappilil, Phys. Rev. D **96**, no.5, 055031 (2017) doi:10.1103/PhysRevD.96.055031 [arXiv:1707.00008 [hep-ph]].
- [69] M. Zhang, Phys. Rev. D **104**, no.5, 055008 (2021) doi:10.1103/PhysRevD.104.055008 [arXiv:2104.06988 [hep-ph]].
- [70] E. Izaguirre, T. Lin and B. Shuve, Phys. Rev. Lett. **118**, no.11, 111802 (2017) doi:10.1103/PhysRevLett.118.111802 [arXiv:1611.09355 [hep-ph]].
- [71] S. Gori, G. Perez and K. Tobioka, JHEP **08**, 110 (2020) doi:10.1007/JHEP08(2020)110 [arXiv:2005.05170 [hep-ph]].
- [72] G. Raffelt and D. Seckel, Phys. Rev. Lett. **60**, 1793 (1988) doi:10.1103/PhysRevLett.60.1793
- [73] C. H. V. Chang, C. R. Chen, S. Y. Ho and S. Y. Tseng, Phys. Rev. D **104**, no.1, 015030 (2021) doi:10.1103/PhysRevD.104.015030 [arXiv:2102.05012 [hep-ph]].
- [74] A. Alloul, N. D. Christensen, C. Degrande, C. Duhr and B. Fuks, Comput. Phys. Commun. **185**, 2250-2300 (2014) doi:10.1016/j.cpc.2014.04.012 [arXiv:1310.1921 [hep-ph]].
- [75] J. Alwall, R. Frederix, S. Frixione, V. Hirschi, F. Maltoni, O. Mattelaer, H. S. Shao, T. Stelzer, P. Torrielli and M. Zaro, JHEP **07**, 079 (2014) doi:10.1007/JHEP07(2014)079 [arXiv:1405.0301

- [hep-ph]].
- [76] T. Sjostrand, S. Mrenna and P. Z. Skands, *Comput. Phys. Commun.* **178**, 852-867 (2008) doi:10.1016/j.cpc.2008.01.036 [arXiv:0710.3820 [hep-ph]].
- [77] J. de Favereau *et al.* [DELPHES 3], *JHEP* **02**, 057 (2014) doi:10.1007/JHEP02(2014)057 [arXiv:1307.6346 [hep-ex]].
- [78] T. Yang, S. Qian, Z. Guan, C. Li, F. Meng, J. Xiao, M. Lu and Q. Li, *Phys. Rev. D* **104**, no.9, 093003 (2021) doi:10.1103/PhysRevD.104.093003 [arXiv:2107.13581 [hep-ph]].
- [79] G. Haghightat and M. Mohammadi Najafabadi, *Nucl. Phys. B* **980**, 115827 (2022) doi:10.1016/j.nuclphysb.2022.115827 [arXiv:2106.00505 [hep-ph]].
- [80] Y. L. Dokshitzer, G. D. Leder, S. Moretti and B. R. Webber, *JHEP* **08**, 001 (1997) doi:10.1088/1126-6708/1997/08/001 [arXiv:hep-ph/9707323 [hep-ph]].
- [81] M. Wobisch and T. Wengler, [arXiv:hep-ph/9907280 [hep-ph]].
- [82] G. Cowan, K. Cranmer, E. Gross and O. Vitells, *Eur. Phys. J. C* **71**, 1554 (2011) [erratum: *Eur. Phys. J. C* **73**, 2501 (2013)] doi:10.1140/epjc/s10052-011-1554-0 [arXiv:1007.1727 [physics.data-an]].
- [83] J. P. Lees *et al.* [BaBar], *Phys. Rev. Lett.* **128**, no.13, 131802 (2022) doi:10.1103/PhysRevLett.128.131802 [arXiv:2111.01800 [hep-ex]].
- [84] D. d'Enterria, [arXiv:2102.08971 [hep-ex]].
- [85] S. Ganguly, B. Mukhopadhyaya and S. Roy, [arXiv:2204.07920 [hep-ph]].
- [86] N. Bartosik *et al.* [Muon Collider], [arXiv:2203.07964 [hep-ex]].
- [87] R. L. Workman *et al.* [Particle Data Group], *PTEP* **2022**, 083C01 (2022) doi:10.1093/ptep/ptac097
- [88] B. Abi *et al.* [Muon g-2], *Phys. Rev. Lett.* **126**, no.14, 141801 (2021) doi:10.1103/PhysRevLett.126.141801 [arXiv:2104.03281 [hep-ex]].
- [89] S. Borsanyi, Z. Fodor, J. N. Guenther, C. Hoelbling, S. D. Katz, L. Lellouch, T. Lippert, K. Miura, L. Parato and K. K. Szabo, *et al.* *Nature* **593**, no.7857, 51-55 (2021) doi:10.1038/s41586-021-03418-1 [arXiv:2002.12347 [hep-lat]].
- [90] F. Abudinén *et al.* [Belle-II], *Phys. Rev. Lett.* **125**, no.16, 161806 (2020) doi:10.1103/PhysRevLett.125.161806 [arXiv:2007.13071 [hep-ex]].
- [91] X. Cid Vidal, A. Mariotti, D. Redigolo, F. Sala and K. Tobioka, *JHEP* **01**, 113 (2019) [erratum: *JHEP* **06**, 141 (2020)] doi:10.1007/JHEP01(2019)113 [arXiv:1810.09452 [hep-ph]].